Research Article

Petrogenesis and tectonic implications of the late Paleoproterozoic A-type rhyolites at the southwestern North China Craton

Lanyin Pang [a,b,c], Yanyan Zhou [d,e], Xinyu Gao [f], Xiaoqin Deng [g], Junhong Zhao [h], Taiping Zhao [a,c,*]

[a] *Key Laboratory of Mineralogy and Metallogeny, Guangzhou Institute of Geochemistry, Chinese Academy of Sciences, Guangzhou 510640, China*
[b] *University of Chinese Academy of Sciences, Beijing 100049, China*
[c] *CAS Center for Excellence in Deep Earth Science, Guangzhou 510640, China*
[d] *State Key Laboratory of Lithospheric Evolution, Institute of Geology and Geophysics, Chinese Academy of Sciences, Beijing 100029, China*
[e] *Innovation Academy for Earth Science, Chinese Academy of Sciences, Beijing 100029, China*
[f] *Guangdong polytechnic of water resources and electric engineering, Guangzhou 510635, China*
[g] *Guangdong Provincial Key Laboratory of Microbial Culture Collection and Application, State Key Laboratory of Applied Microbiology Southern China, Guangdong Institute of Microbiology, Guangdong Academy of Sciences, Guangzhou 510070, China*
[h] *State Key Laboratory of Geological Processes and Mineral Resources, China University of Geosciences, Wuhan 430074, China*

A R T I C L E   I N F O

A B S T R A C T

The late Paleoproterozoic A-type granitoids are important for constraining of the lithotectonic and geodynamic processed involved in the creation of continental crust. The newly identified late Paleoproterozoic felsic extrusive rocks from the southwestern margin of the North China Craton (NCC) consist of rhyolites which show melting corrosion structure, autoclastic texture and fiber structure of mineral grains and have weighted mean SIMS zircon U—Pb ages of 1794.7 ± 3.6 Ma to 1780.3 ± 5.6 Ma. The rhyolite samples show high SiO_2 (67.59–74.38 wt%) and $K_2O + Na_2O$ (3.68–11.10 wt%), and low MgO (0.05–1.17 wt%), CaO (0.19–2.58 wt%) and P_2O_5 (0.08–0.16 wt%). They display aluminous A-type granite/rhyolite geochemical compositions, such as high A/CNK (0.78–1.23), $FeO^T/(FeO^T + MgO)$ (0.81–0.99) and 10000Ga/Al (2.32–4.03) ratios, and high Zr + Nb + Ce + Y (824–1272 ppm) concentrations, as well as high zirconium saturation temperatures (T_{Zr} = 873–964 °C). These signatures, along with their low $\varepsilon_{Hf}(t)$ (−3.6 to −1.5) and $\varepsilon_{Nd}(t)$ values (−4.31 to −3.31) and old two-stage Hf model ages (T_{DM}^C = 2.70–2.57 Ga), indicate that the rhyolites were derived from partial melting of the Neoarchean felsic basement rocks. These volcanic rocks also have low zircon $\delta^{18}O$ values ranging from 1.5‰ to 6.8‰, which were inherited from the Neoarchean ^{18}O-depleted basement rocks that underwent high-T hydrothermal alteration, rather than resulted from contamination or later high-T water/rock interaction. The rhyolite rocks in this study, the earliest igneous rocks in the southwestern NCC after the Paleoproterozoic consolidation of the crystalline basement, were formed in a rift setting, marking the initial breakup of the Guyuan Rift in the southwestern NCC. The rhyolite rocks in combination with the Xiong'er volcanic rocks in the southern NCC mark the initial rifting of the NCC (Xiong'er Rift and Guyuan Rift) after cratonization (~1.85–1.8 Ga). The youngest retrograde metamorphism (1.80–1.79 Ga) in the NCC indicates that the transition from post-orogenic to intracontinental rift setting occurred at ca. 1.79 Ga.

© 2021 Elsevier B.V. All rights reserved.

1. Introduction

The North China Craton (NCC) is one of the oldest continental blocks in the world, containing rocks as old as 3.85 Ga (e.g., Liu et al., 2009a). It has a complicated evolutionary history recording multi-stages of crustal growth and almost all major Precambrian geological events in the world (e.g., Zhai and Santosh, 2011). The amalgamation of the Eastern and Western blocks along the Trans-North China Orogen marked the

final cratonization of the NCC at ca. 1.85 Ga (e.g., Zhang et al., 2007; Zhao et al., 2012), followed by intensive extension that generated several continental rifts or aulacogens during the late Paleoproterozoic era (Zhai et al., 2015), including the Yanliao Rift in the north-central, the Zhaertai-Bayan Obo Rift in the north, and the Xiong'er Rift in the south. Voluminous extension-related magmatic rocks were developed, such as ca.1.78 Ga Xiong'er volcanic rocks and mafic dyke swarms (Peng et al., 2008; Zhao et al., 2002), ca.1.8–1.6 Ga A-type granites (Deng et al., 2016; Zhao and Zhou, 2009), ca.1.75–1.68 Ga anorthosite-mangerite-alkali granitoid-rapakivi granite suite (Zhang et al., 2007), and ca.1.77 Ga Donggouzi gabbroic dike (Han et al., 2020). Nevertheless, the specific transition time from orogeny to the intracontinental rift in the

* Corresponding author at: Key Laboratory of Mineralogy and Metallogeny, Guangzhou Institute of Geochemistry, Chinese Academy of Sciences, Guangzhou 510640, China.
   E-mail address: tpzhao@gig.ac.cn (T. Zhao).

NCC remains controversial due to lack of precise dating results for the late Paleoproterozoic magmatism (e.g., Cawood and Hawkesworth, 2014).

Loiselle and Wones (1979) proposed that A-type granites are alkaline, anhydrous, and anorogenic. They have high alkali and low CaO, MgO and Al_2O_3, are rich in HFSE (i.e., Zr, Nb, Ce, Y), Ba and Sr, and are strongly depleted in P and Ti, exhibit prominent negative Eu anomalies (e.g., Whalen et al., 1987). A-type granites/rhyolites are compositionally diverse. For example, they may be peralkaline and contain sodium-rich mafic minerals or be weakly peraluminous to mataluminous without sodium-rich mafic minerals (King et al., 1997).

A-type granite/rhyolite is generally formed in crustal extensional tectonic setting, such as post-orogenic, anorogenic or mantle plume-related environments (e.g., Patiño Douce, 1997; Shellnutt and Zhou, 2007; Yang et al., 2006). They were rarely identified in the Archean and early to middle Paleoproterozoic, but widespread in the late Paleoproterozoic units (e.g., Whalen et al., 1987). The occurrence of A-type granites/rhyolites in most Precambrian blocks implies the beginning of the craton stabilization after the ending of the orogenic processes (e.g., Drüppel et al., 2009), indicating a geodynamic transition of the continental evolution of the Earth (e.g., Loiselle and Wones, 1979; Whalen et al., 1987).

The late Paleoproterozoic geological evolution of the southwestern margin of the NCC has not been well constrained relative to the other regions because of the rare occurrence of Precambrian basement and thus hindering recognition of the pale-tectonic setting (Zhang et al., 2015 and reference therein). The newly identified three series of late Paleoproterozoic A-type rhyolites (Gao et al., 2013; Wang et al., 2019; Xu et al., 2014; You et al., 2014) represent the earliest magmatism in the southwestern margin of the NCC after the Paleoproterozoic consolidation of the crystalline basement, and thus have great geological significance to constrain its tectonic evolution.

In this paper, we present systematic petrography, geochronological, whole-rock major and trace elemental, Sm—Nd isotopic and zircon Hf—O isotopic data for the late Paleoproterozoic A-type rhyolites from the southwestern margin of the NCC to address their precise emplacement ages, petrogenesis and tectonic settings, as well as the correlation among the late Paleoproterozoic magmatism in the NCC.

2. Geological background

The NCC is bounded by the Central Asian Orogenic Belt to the north, the Qinling-Dabie Orogenic Belt to the south, and the Su-Lu Orogenic Belt to the east (Fig. 1b). Its early Precambrian basement consists of three tectonic units, the Eastern and Western blocks, and the intervening Trans-North China Orogen (Zhao et al., 2001, 2012). The Western Block was formed by the amalgamation of the Yinshan and Ordos blocks along the Khondalite Belt at ca.1.95 Ga, and subsequently collided with the Eastern Block along the Trans-North China Orogen at ca.1.85 Ga (Zhao et al., 2012). The Khondalite Belt is predominated by supercrustal metasedimentary sequences, associated with minor mafic granulites, TTG gneisses, amphibolites, as well as *syn*-tectonic S-type granites and charnockites (Yin et al., 2011). The Trans-North China Orogen, a classical continent-continent collisional belt, mainly consists of Neoarchean to Paleoproterozoic TTG gneisses, Paleoproterozoic meta-supracrustal rocks, granites rocks and meta-mafic dykes (Zhao et al., 2001, 2012). The basement rocks of the NCC are composed mainly of the Neoarchean-Paleoproterozoic tonalitic-trondhjemitic-granodioritic (TTG) gneisses, metamorphosed supracrustal rocks (including greenstone belts) and K-rich granitic rocks, associated with minor sporadic Paleo-Mesoarchean gneiss complexes (e.g., Liu et al., 2009a; Zhao et al., 2001). They are overlain by the late Paleoproterozoic to Neoproterozoic unmetamorphosed sedimentary covers, such as the Xiong'er, Ruyang-Luoyu, Guandaokou, Wufoshan, and Luanchuan groups in the southern part, the Changcheng, Jixian and Qingbaikou groups in the north-central part, the Bayan Obo and Zhaertai groups in the northwestern part, and the Huangqikou, Wangquankou and Zhengmuguan formations in the western margin (e.g., Hou et al., 2006; Hu et al., 2014, 2016; Wang et al., 1992). The late Paleoproterozoic magmatic rocks are mainly composed of 1.8–1.75 Ga Xiong'er volcanic rocks, mafic dykes and granitic rocks (Peng et al., 2008; Zhao et al., 2002).

The Ordos Block is bounded by the Paleoproterozoic Khondalite Belt to the north, the Paleozoic Kunlun-Qilian orogenic belt to the west, the Mesozoic Qinling orogenic belt to the south and the Trans-North China Orogen to the east (Fig. 1b). It is a stable block without strong deformation and earthquakes and has a ~ 200 km thick lithosphere with low heat flow and high-velocity anomalies (Kusky and Mooney, 2015; Zhang et al., 2015). The Ordos Block is covered by the thick Phanerozoic sediments with sporadical outcrop of Precambrian strata and magmatic rocks, but drill cores reveal that it has typical double-layer crustal structure characterized by the early Precambrian crystalline basement and the late Paleoproterozoic to Phanerozoic sedimentary cover (Zhang et al., 2015). The crystalline basement is composed of late Archean to Paleoproterozoic granulite-facies rocks (Zhang et al., 2015 and reference
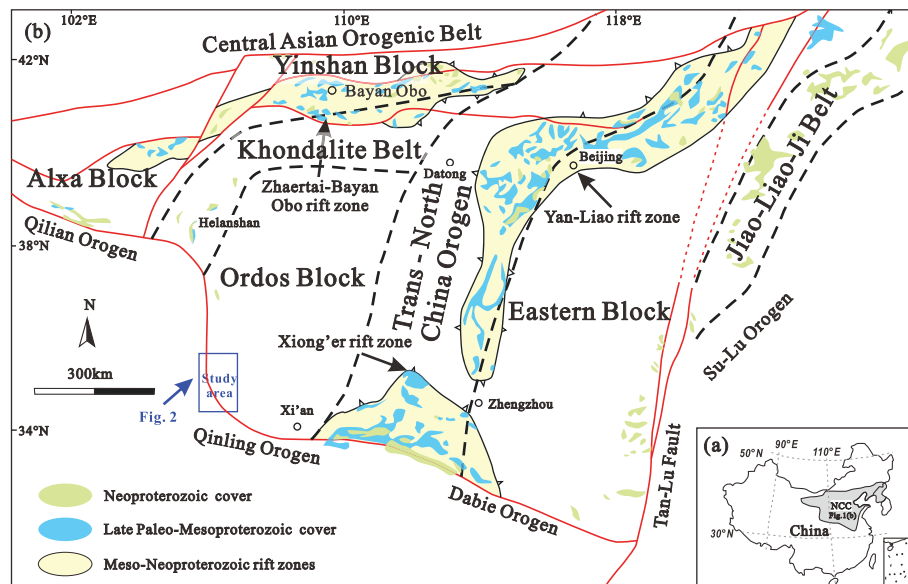

Fig. 1. (a) Location of the North China Craton (NCC). (b) Simplified map of the tectonic subdivision of the NCC (modified by Hu et al. (2014)).

therein), whereas the Precambrian sedimentary cover, up to 4000–6000 m thick, consists of the Statherian, Calymmian and little Ediacaran strata (the Ectasian to Cryogenian strata is absent) as revealed by the north-south and east-west direction seismic profiles (Hu et al., 2016).

The late Paleoproterozoic magmatic rocks are dominantly distributed in the southwestern margin of the Ordos Block and comprise a small amount of diabase and three series of rhyolites in the Baijiagou, Baojiashan and Shizuizi regions (Xu et al., 2014; You et al., 2014). Che and Wang (1985) defined them as Mesozoic-Cenozoic according to the age of surrounding rocks, whereas zircon geochronology study on these rocks obtained results of late Paleoproterozoic (Gao et al., 2013; Xu et al., 2014; You et al., 2014; this study). The study area is located at the Baoji City of Shanxi Province and Guyuan City of Ningxia Hui Autonomous Region, southwestern Ordos Block (Fig. 2a). The Baijiagou rhyolite, located at Long Country of Shaanxi Province, extends northeastern direction with an exposure length of about 80 m (Fig. 2b). The host rocks are mainly of limestone of the Upper Ordovician Beiguoshan Formation and loess of Quaternary. The contact relationship between the rhyolite and the early Precambrian geological body is not clear. The Shizuizi rhyolite, 50 m wide, is located in the Jingyuan country, Ningxia Hui Autonomous Region, with extending direction of northwest-southeastern direction and was covered by Quaternary sediments (Figs. 2c, 4a). The Baojiashan rhyolite is also located in the Long Country, Shaanxi Province, 15 km away (straight-line distance) from the Baijiagou rhyolite in the northwest side (Fig. 2d). It is 1.3 km long and 250 m wide with NW-SW direction. The west side of the rhyolite is burgundy clastic rocks of the Lower Cretaceous Heshangpu Formation, while the east is the Sinian System dolomite. Because of the widely Quaternary sediment coverage, the contact relationship between the rhyolite and the ancient geologic body can't be seen in the field, either.

3. Petrography and sampling location

The Baijiagou rhyolite shows porphyritic texture and massive structure (Fig. 3a-b). The phenocryst minerals (30 vol%) consist of K-feldspar (~15 vol%), quartz (~10 vol%), and plagioclase (less than 5 vol%).

Subhedral K-feldspar preserves noticeable autoclastic texture and experienced weak kaolinization and carbonatization (Fig. 3d, e). Quartz often occurs as xenomorphic granular texture, and they are characterized frequently by melting corrosion structure (Fig. 3c, f). Most plagioclase grains display autoclastic texture and locally show melting corrosion structure (Fig. 3e). The groundmass (70 vol%) has the same minerals as the phenocrysts with cryptocrystalline and felsitic texture (Fig. 3e). The samples also preserve minor vesicles (Fig. 3c), Fe—Ti oxides, apatite and zircon (<1%). Noticeably, sample BJG-3 presents rhyolitic structure (Fig. 3f).

The Shizuizi rhyolite is lithologically similar to the Baijiagou rhyolite (Fig. 4a-b). The phenocrysts mainly consist of K-feldspar (12 vol%), quartz (12 vol%) and plagioclase (less than 5 vol%) associated with minor biotite and amphibole (less than 1 vol%). K-feldspar phenocrysts display autoclastic texture and melting corrosion structure (Fig. 4c). Quartz grains generally show rounded or embayed margins (Fig. 4c, d). They also have minor vesicles (1 vol%) and amygdales (less than 1 vol%) (Fig. 4c, d).

The Baojiashan rhyolite shows clear vesicular textures in the outcrop (Fig. 5b). The phenocryst minerals, accounting for about 35 vol%, consist of K-feldspar (20 vol%), quartz (10 vol%) and minor plagioclase (less than 5 vol%). Subhedral K-feldspars present autoclastic melting corrosion textures (Fig. 5f). Quartzes can be divided into two categories, xenomorphic granular quartz with melting corrosion margins and microscopic crystals arranged in slender fibers, arborization or radial patterns (Fig. 5c-f). These characteristics indicate that the rocks were formed in a rapidly cooling environment. The groundmass (65 vol%) has the same mineral assemblages, but contains more Fe—Ti oxides and minor vesicles and amygdales (Fig. 5f).

Four, three, and six samples respectively collected from the Baijiagou, Shizuizi, and Baojiashan rhyolites were carried out for analyzing of whole-rock major and trace elements. One representative sample from each of the three rhyolites was conducted for zircon SIMS U—Pb dating, Lu—Hf isotopic, and O isotopic analyses. Two representative samples from each of the three rhyolites were conducted for the whole rock Sm—Nd isotopic analysis.
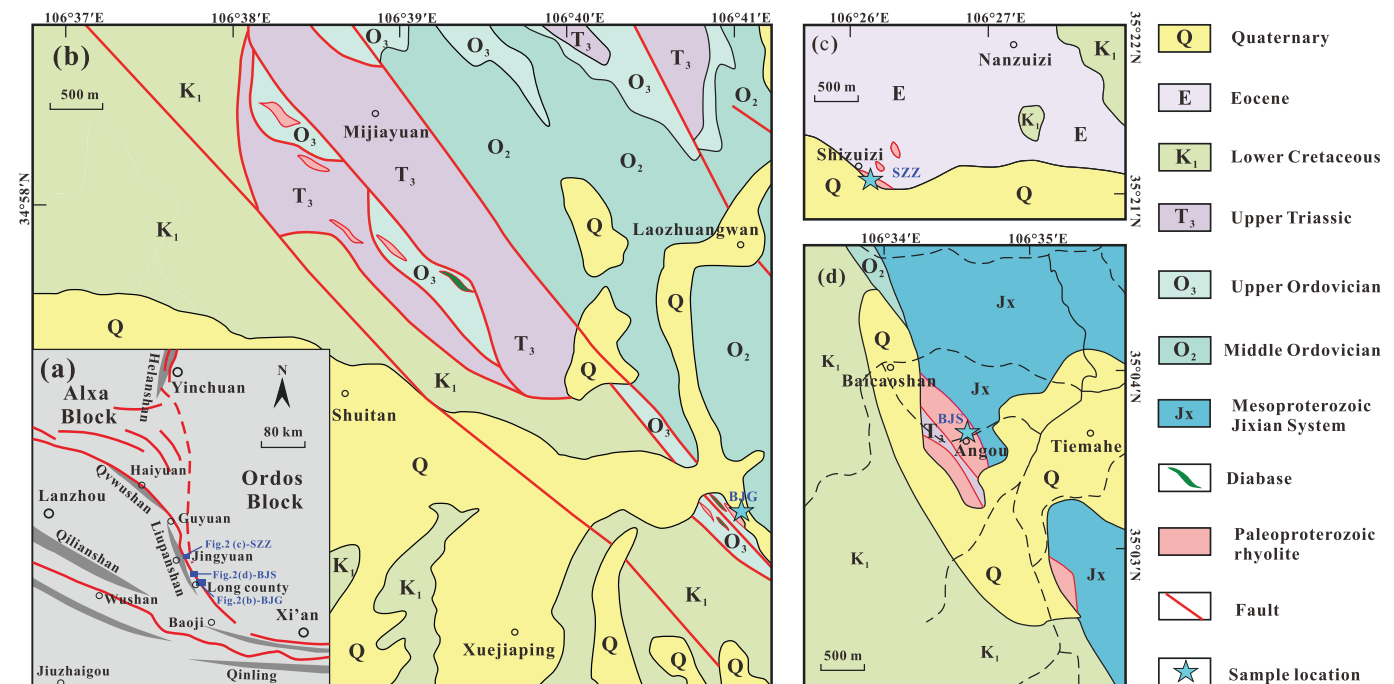

Fig. 2. (a) Simplified tectonic map of the southwestern margin of the Ordos Block. BJG-the Baijiagou rhyolite; SZZ-the Shizuizi rhyolite; BJS-the Baojiashan rhyolite. Simplified geological map of the (b) Baijiagou rhyolite (modified by You et al., 2014), (c) Shizuizi rhyolite (modified by Gao et al., 2013) and (d) Baojiashan rhyolite (modified by Wang et al., 2019).
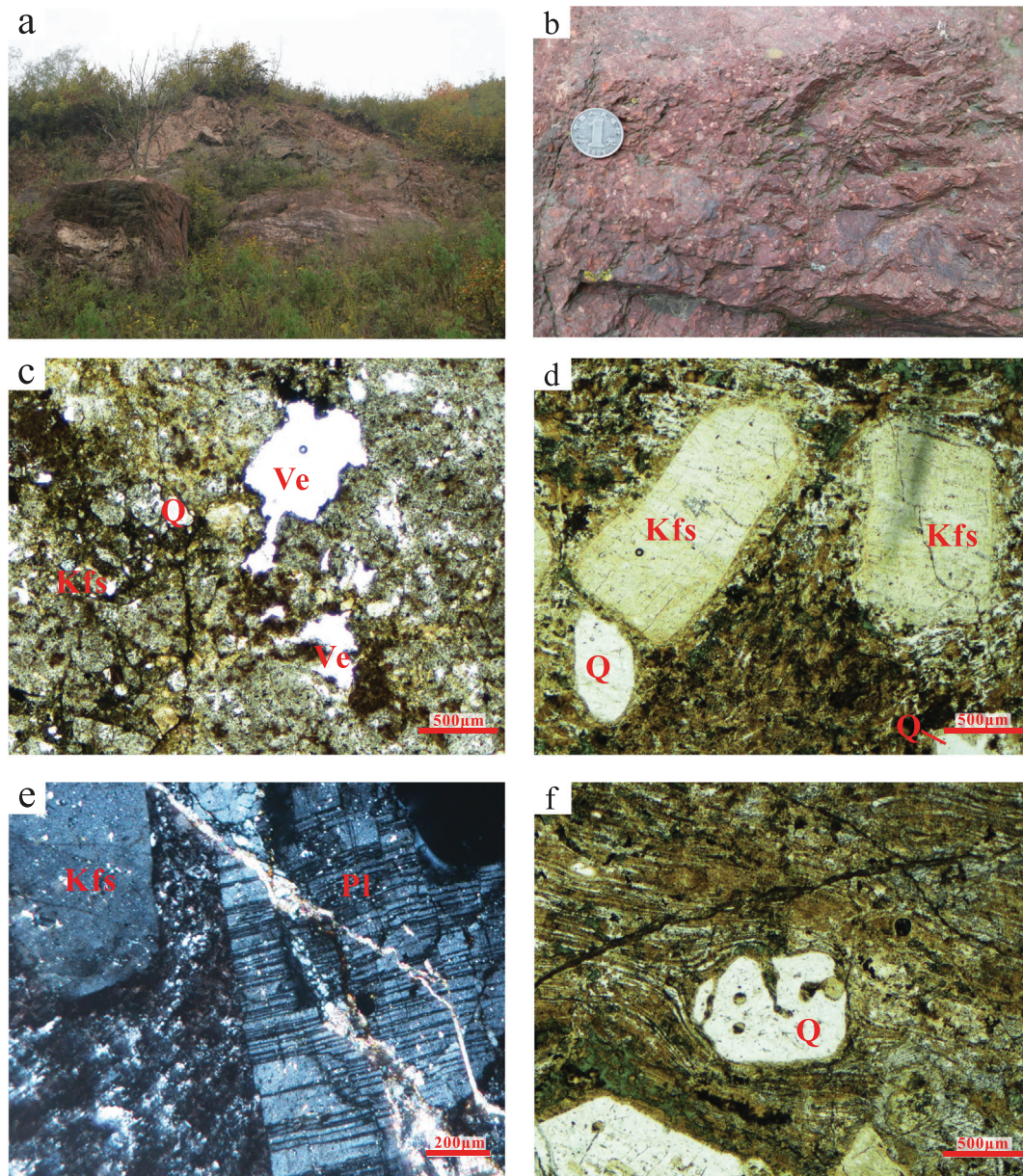
Fig. 3. Field photographs (a-b) and photomicrographs under cross-polarized light (c-f) showing the petrographic characteristics of the Baijiagou rhyolites. Mineral abbreviations: Kfs, k-feldspar; Pl, plagioclase; Q, quartz; Ve, vesicle amygdales.

4. Analytical methods

4.1. Zircon SIMS U—Pb dating

Zircons were extracted using conventional density and magnetic separation. Zircon grains were handpicked under a binocular microscope. The zircon grains were mounted in epoxy resin, polished to half their thickness, and then photographed in transmitted and reflected light. The morphology and internal structures of zircons were examined using cathodoluminescence (CL) imaging before U-Pb-Hf isotopic analysis. The CL images were obtained using an EMPA-JXA-8100 scanning electron microscope at the Guangzhou Institute of Geochemistry, Chinese Academy of Sciences (GIGCAS).

SIMS zircon U—Pb analyses were performed on a Cameca IMS-1280HR ion microprobe at Guangzhou Institute of Geochemistry, Chinese Academy of Sciences (GIGCAS) following procedures described by Li et al. (2009). The O_2-primary ion beam was accelerated at 13 kV, with an intensity of 10 nA. The ellipsoidal spot is about 20×30 μm in size. Positive secondary ions were extracted with a 10 kV potential. Calibration of Pb/U ratios is based on an observed linear relationship between ln ($^{206}Pb/^{238}U$) and ln ($^{238}U^{16}O_2/^{238}U$). Measured compositions were corrected for common Pb using non-radiogenic ^{204}Pb. Analyses of the standards Plesovice and Qinghu were interspersed with unknowns. The age calculations and concordia plots were made using ISOPLOT (ver. 3.0) (Ludwig, 2003).

4.2. Zircon oxygen isotopes

Zircon in-situ O isotopes were analyzed using Cameca IMS 1280-HR at State Key Laboratory of Isotope Geochemistry in GIGCAS, Guangzhou. Analytical procedures are the same as those described by Li et al. (2010). The Cs + primary ion beam was accelerated at 10 kV, with an intensity of ca. 2 nA (Gaussian mode with a primary beam aperture of 200 μm to reduce aberrations) and rastered over a 10 μm area. The analysis spot
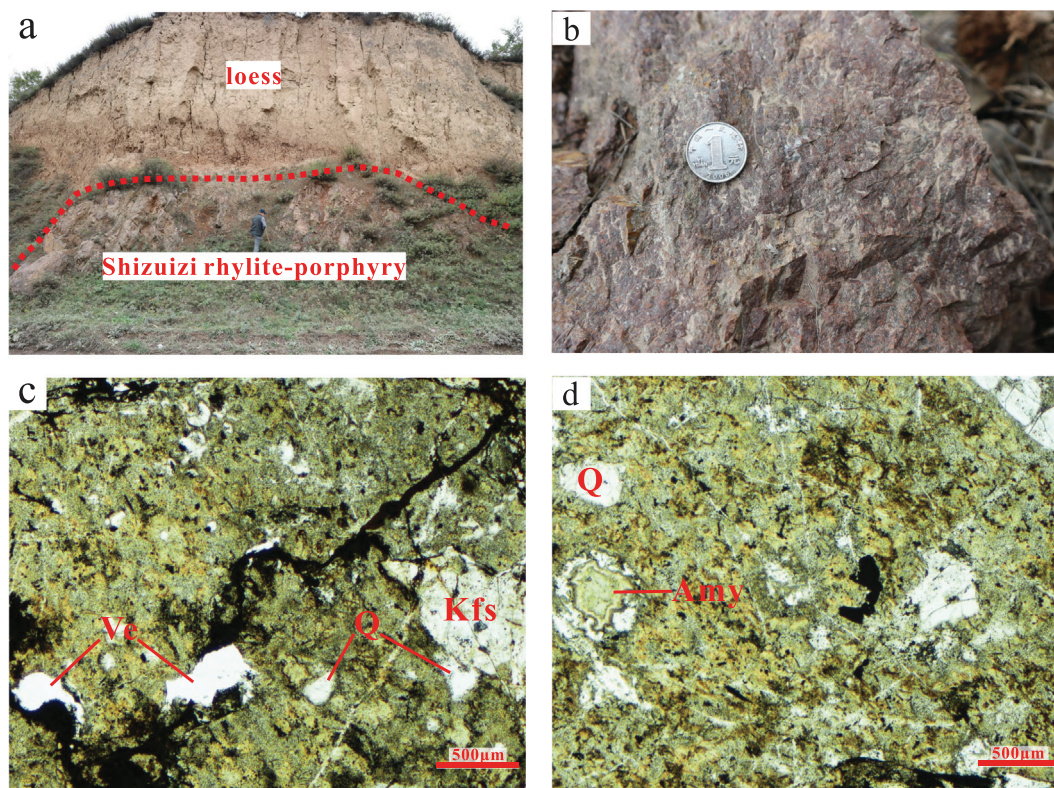
Fig. 4. Field photographs (a–b) and photomicrographs under cross-polarized light (c–d) showing the petrographic characteristics of the Shizuizi rhyolites. Mineral abbreviations: Kfs, k-feldspar; Q, quartz; Ve, vesicles; Amy, amygdales.

was about 20 μm in diameter (10 μm beam diameter + 10 μm raster). Oxygen isotopes were measured in multi-collector mode using two off-axis Faraday cups. The NMR (Nuclear Magnetic Resonance) probe was used for magnetic field control with stability better than 2.5 ppm over 16 h on mass 17. One analysis takes ~3.5 min consisting of pre-sputtering (~ 30 s), 120 s of automatic tuning of the secondary beam, and 64 s of analysis. The instrumental mass fractionation (IMF) was corrected using in-house zircon standard Penglai with a recommended $\delta^{18}O$ value of 5.33 ± 0.07‰ with reference to the Vienna standard mean oceanic water (VSMOW) that has a recommended $^{18}O/^{16}O$ ratio of 0.0020052 (Li et al., 2010). The measured $^{18}O/^{16}O$ ratios for samples (raw data) were firstly normalized relative to the VSMOW and then corrected for IMF (Li et al., 2010). The internal precision of a single analysis was generally better than ± 0.20‰ (2σ standard error) for $\delta^{18}O$ values. During analysis, a second zircon standard Qinghu was measured as an unknown to ascertain the veracity of the IMF. Nine measurements of Qinghu zircon standard yield a weighted mean of $\delta^{18}O = 5.54 \pm 0.14$‰ (2SD). These values are in good agreement with errors with a reported value of 5.4 ± 0.2‰ (Li et al., 2013).

4.3. Zircon Lu—Hf isotope analysis

Experiments of in situ Hf isotope ratio analysis were conducted using a Neptune Plus MC-ICP-MS (Thermo Fisher Scientific, Germany) in combination with a Geolas HD excimer ArF laser ablation system (Coherent, Göttingen, Germany) that was hosted at the Wuhan Sample Solution Analytical Technology Co., Ltd., Hubei, China. A "wire" signal smoothing device is included in this laser ablation system, by which smooth signals are produced even at very low laser repetition rates down to 1 Hz (Hu et al., 2015). Helium was used as the carrier gas within the ablation cell and was merged with argon (makeup gas) after the ablation cell. Small amounts of nitrogen were added to the argon makeup gas flow for the improvement of sensitivity of Hf isotopes (Hu et al., 2012). All data were acquired on zircon in single spot ablation

mode at a spot size of 44 μm. The energy density of laser ablation that was used in this study was ~7.0 J/cm². Each measurement consisted of 20 s of acquisition of the background signal followed by 50 s of ablation signal acquisition. Detailed operating conditions for the laser ablation system and the MC-ICP-MS instrument and analytical method are the same as description by Hu et al. (2012).

The major limitation to accurate in situ zircon Hf isotope determination by LA-MC-ICP-MS is the very large isobaric interference from ^{176}Yb and, to a much lesser extent ^{176}Lu on ^{176}Hf. We applied the directly obtained βYb value from the zircon sample itself in real-time in this study. Off-line selection and integration of analyte signals and mass bias calibrations were performed using ICPMS DataCal (Liu et al., 2010).

4.4. Whole-rock major and trace element analyses

Individual samples, selected from least altered and homogeneous parts, were crushed and milled to powder of 200 mesh. Whole-rock major and trace element concentrations of ten representative fresh or weakly altered amphibolite samples were analyzed at the State Key Laboratory of Isotope Geochemistry, GIGCAS. Major element analyses were performed by X-ray fluorescence spectrometry (XRF) on fused glass beads with the analytical uncertainties at ±1–2%. The detailed analytical procedure is described in Li et al. (2006). Trace elements, including REE, were analyzed using a Perkin-Elmer Sciex Elan 6000 inductively coupled plasma mass spectrometry (ICP-MS). A set of USGS and Chinese national rock standards, including BHVO-2, GSR-1, GSR-2, GSR-3, AGV-2, W-2 and SARM-4, were chosen for calibration, with a precision better than 5% for most elements.

4.5. Whole-rock Sm—Nd isotope analysis

Whole-rock Sm—Nd isotopic compositions were analyzed using a FinniganMAT-262 multi-collector spectrometer at GIGCAS. Sample powders were dissolved in Teflon bombs using HF + HClO₄ after
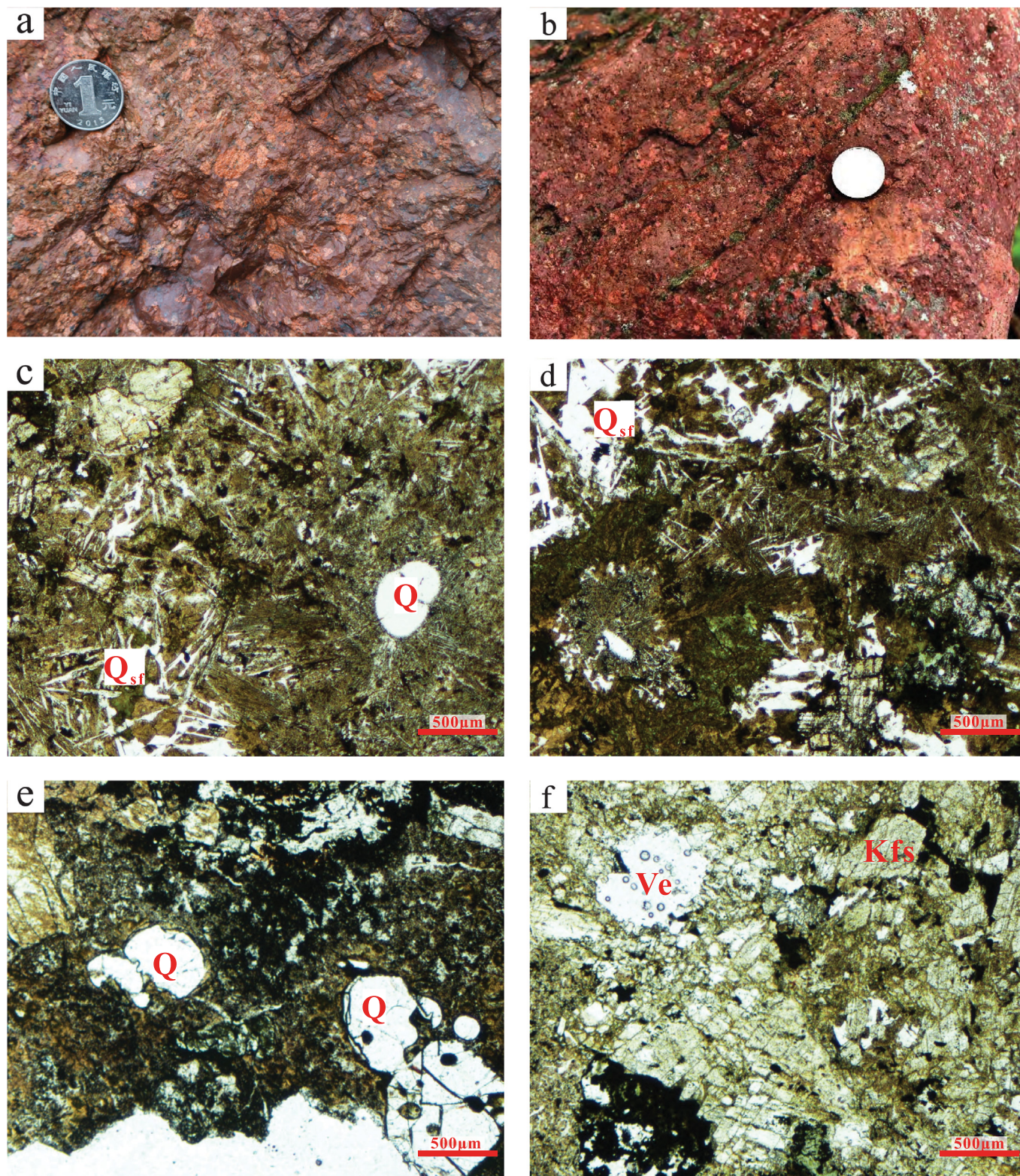
Fig. 5. Field photographs (a-b) and photomicrographs under cross-polarized light (c-f) showing the petrographic characteristics of the Baojiashan rhyolites. Mineral abbreviations: Kfs, k-feldspar; Q, quartz; Q_{sf}, crystals quartz of slender fibers; Ve, vesicles.

Table 1
SIMS U—Pb dating results of zircons from the Baijiagou, Shizuizi and Baojiashan rhyolites.

Sample Spot	Contents (ppm)				Isotopic ratios						Isotopic ages (Ma)						Concor
	U	Th	Pb	Th/U	$^{207}Pb/^{206}Pb$	±σ	$^{207}Pb/^{235}U$	±σ	$^{206}Pb/^{238}U$	±σ	$^{207}Pb/^{206}Pb$	±σ	$^{207}Pb/^{235}U$	±σ	$^{206}Pb/^{238}U$	±σ	
	ppm	ppm	ppm			%		%		%							%
BJG-4																	
1	65	46	27	0.70	0.1105	0.47	4.7340	1.59	0.3107	1.52	1807.7	8.5	1773.3	13.4	1744.2	23.3	98
2	54	33	22	0.62	0.1097	0.52	4.8047	1.60	0.3177	1.51	1794.1	9.4	1785.7	13.5	1778.5	23.5	100
3	56	34	23	0.61	0.1090	0.52	4.7581	1.59	0.3165	1.50	1783.6	9.5	1777.5	13.4	1772.4	23.3	100
4	59	36	24	0.62	0.1092	0.93	4.7717	1.78	0.3170	1.52	1785.8	16.8	1779.9	15.1	1774.9	23.7	100
5	83	62	35	0.75	0.1090	0.46	4.7998	1.65	0.3195	1.59	1782.1	8.4	1784.9	14.0	1787.2	24.8	100
6	76	53	32	0.70	0.1100	0.45	4.7813	1.58	0.3151	1.52	1800.2	8.1	1781.6	13.4	1765.8	23.5	99
7	62	41	26	0.65	0.1091	0.57	4.8271	1.64	0.3209	1.54	1784.6	10.4	1789.6	13.9	1793.9	24.2	100
8	62	41	26	0.66	0.1106	0.51	4.8337	1.70	0.3168	1.62	1810.1	9.3	1790.8	14.4	1774.2	25.2	99
9	54	34	22	0.64	0.1100	0.57	4.8205	1.63	0.3180	1.53	1798.6	10.4	1788.5	13.8	1779.8	23.8	100
10	54	34	22	0.63	0.1095	0.54	4.7934	1.62	0.3174	1.53	1791.9	9.9	1783.8	13.7	1776.8	23.8	100
11	63	43	26	0.68	0.1099	0.55	4.8048	1.82	0.3172	1.73	1797.1	10.0	1785.7	15.4	1776.0	26.9	99
12	76	56	32	0.74	0.1102	0.68	4.7520	1.68	0.3129	1.53	1801.9	12.4	1776.5	14.2	1754.9	23.5	99
13	75	53	31	0.71	0.1102	0.47	4.8521	1.57	0.3194	1.50	1802.1	8.4	1794.0	13.3	1787.0	23.5	100
14	83	62	35	0.75	0.1100	0.50	4.7698	1.61	0.3145	1.53	1799.5	9.0	1779.6	13.6	1762.7	23.7	99
15	77	56	32	0.72	0.1098	0.44	4.7440	1.61	0.3133	1.54	1796.6	8.0	1775.0	13.6	1756.8	23.8	99
16	92	86	38	0.94	0.1086	0.41	4.5659	1.56	0.3048	1.50	1776.6	7.5	1743.1	13.1	1715.2	22.7	98
17	65	44	27	0.68	0.1098	0.47	4.8414	1.57	0.3197	1.50	1796.5	8.5	1792.1	13.3	1788.4	23.5	100
18	62	41	25	0.66	0.1095	0.56	4.7410	1.60	0.3141	1.50	1790.6	10.1	1774.5	13.5	1760.9	23.2	99
19	72	50	29	0.69	0.1104	0.76	4.7661	1.89	0.3132	1.74	1805.4	13.7	1779.0	16.0	1756.5	26.7	99
20	66	44	27	0.67	0.1096	0.47	4.7517	1.59	0.3145	1.52	1792.2	8.5	1776.4	13.4	1763.0	23.5	99
21	61	39	25	0.63	0.1102	0.49	4.7818	1.59	0.3148	1.51	1802.2	9.0	1781.7	13.5	1764.3	23.4	99
22	59	38	24	0.65	0.1103	0.48	4.8381	1.58	0.3180	1.50	1804.9	8.7	1791.6	13.3	1780.1	23.4	99
23	60	39	25	0.65	0.1097	0.49	4.7862	1.66	0.3164	1.59	1794.4	8.9	1782.5	14.0	1772.4	24.7	99
24	57	34	23	0.59	0.1096	0.49	4.7753	1.58	0.3160	1.50	1792.6	8.9	1780.6	13.4	1770.3	23.3	99
25	93	69	37	0.75	0.1092	0.41	4.5374	1.73	0.3013	1.68	1786.3	7.4	1737.9	14.5	1697.9	25.1	98
SZZ-1																	
1	47	38	20	0.80	0.1084	0.57	4.7670	1.60	0.3190	1.50	1772.1	10.3	1779.1	13.5	1785.1	23.4	100
2	62	48	26	0.79	0.1067	0.67	4.7044	1.65	0.3198	1.51	1743.7	12.2	1768.0	13.9	1788.7	23.6	99
3	35	17	14	0.49	0.1091	0.80	4.7688	1.70	0.3169	1.50	1784.8	14.5	1779.4	14.4	1774.8	23.3	100
4	38	26	15	0.68	0.1103	0.78	4.6985	1.70	0.3090	1.52	1804.3	14.0	1767.0	14.4	1735.6	23.1	98
5	52	39	22	0.76	0.1074	0.95	4.6874	1.78	0.3166	1.50	1755.1	17.3	1765.0	15.0	1773.3	23.3	100
6	47	28	19	0.59	0.1106	0.67	4.8741	1.65	0.3196	1.51	1809.4	12.1	1797.8	14.0	1787.8	23.6	99
7	60	45	25	0.75	0.1092	0.57	4.7233	1.87	0.3137	1.78	1786.3	10.4	1771.4	15.8	1758.7	27.5	99
8	57	36	24	0.63	0.1098	1.02	4.8463	1.85	0.3202	1.54	1795.4	18.4	1793.0	15.7	1790.9	24.1	100
9	56	41	24	0.73	0.1098	0.53	4.8298	1.60	0.3191	1.51	1795.8	9.6	1790.1	13.6	1785.2	23.6	100
10	67	57	29	0.84	0.1121	1.94	4.8565	2.45	0.3141	1.50	1834.1	34.8	1794.8	20.9	1761.1	23.2	98
11	52	34	22	0.66	0.1103	0.73	4.9429	1.71	0.3250	1.55	1804.3	13.3	1809.6	14.6	1814.2	24.5	100
12	48	29	20	0.62	0.1091	0.88	4.8038	1.76	0.3193	1.53	1784.9	15.9	1785.6	14.9	1786.1	23.9	100
13	43	29	18	0.69	0.1096	0.59	4.8533	1.70	0.3210	1.60	1793.6	10.6	1794.2	14.4	1794.7	25.1	100
14	55	48	24	0.87	0.1084	0.58	4.7962	1.76	0.3208	1.66	1773.1	10.6	1784.2	14.9	1793.7	26.1	99
15	49	32	20	0.66	0.1096	0.57	4.8459	1.61	0.3208	1.50	1792.3	10.4	1792.9	13.6	1793.4	23.5	100
16	57	35	23	0.63	0.1099	0.54	4.7380	1.64	0.3125	1.55	1798.6	9.8	1774.0	13.9	1753.2	23.9	99
17	53	43	22	0.80	0.1067	0.86	4.6050	1.83	0.3129	1.62	1744.6	15.6	1750.2	15.4	1754.9	24.9	100
18	42	28	17	0.67	0.1091	0.62	4.7388	1.78	0.3149	1.67	1785.0	11.2	1774.1	15.0	1764.9	25.8	99
19	43	27	17	0.62	0.1095	0.60	4.8001	1.64	0.3179	1.53	1791.2	10.9	1784.9	13.9	1779.5	23.8	100
20	75	65	33	0.87	0.1094	0.46	4.7756	1.60	0.3167	1.53	1788.8	8.3	1780.6	13.5	1773.6	23.8	100
21	54	32	22	0.60	0.1091	0.54	4.7325	1.73	0.3145	1.64	1785.0	9.9	1773.0	14.6	1762.9	25.3	99
22	25	16	10	0.62	0.1076	15.01	4.7347	15.09	0.3192	1.53	1758.5	251.8	1773.4	135.1	1786.0	23.9	99
23	94	79	39	0.84	0.1105	0.48	4.6128	1.58	0.3029	1.50	1806.8	8.7	1751.6	13.3	1705.7	22.6	97
24	82	71	36	0.86	0.1088	0.44	4.8273	1.57	0.3219	1.50	1778.9	8.1	1789.7	13.3	1798.9	23.6	99
25	63	43	26	0.69	0.1093	0.50	4.7852	1.58	0.3177	1.50	1787.0	9.1	1782.3	13.4	1778.3	23.4	100
BJS-3																	
1	33	23	13	0.69	0.1075	0.84	4.5878	1.77	0.3096	1.56	1757.0	15.2	1747.1	14.8	1738.8	23.8	100
2	39	33	16	0.84	0.1084	0.62	4.6185	1.66	0.3089	1.54	1773.1	11.3	1752.6	14.0	1735.5	23.5	99
3	38	25	15	0.65	0.1095	0.64	4.7399	1.68	0.3141	1.55	1790.3	11.6	1774.3	14.2	1760.8	24.0	99
4	52	50	23	0.96	0.1078	0.90	4.6899	1.82	0.3154	1.59	1763.1	16.3	1765.4	15.4	1767.4	24.6	100
5	55	50	23	0.90	0.1091	0.56	4.6152	1.61	0.3068	1.50	1784.6	10.2	1752.0	13.5	1724.8	22.8	98
6	25	15	10	0.62	0.1109	1.03	4.6974	1.83	0.3073	1.51	1813.6	18.7	1766.8	15.5	1727.5	23.0	98
7	51	51	23	1.00	0.1074	0.81	4.7236	1.83	0.3191	1.64	1755.3	14.7	1771.4	15.4	1785.2	25.6	99
8	49	46	21	0.95	0.1091	0.90	4.7454	1.82	0.3156	1.58	1783.9	16.2	1775.3	15.3	1768.0	24.5	100
9	43	33	18	0.77	0.1095	0.74	4.7499	1.73	0.3147	1.57	1790.8	13.4	1776.1	14.6	1763.6	24.2	99
10	61	53	26	0.87	0.1094	0.55	4.7905	1.83	0.3175	1.75	1790.2	9.9	1783.2	15.5	1777.3	27.2	100
11	47	42	20	0.90	0.1061	0.79	4.6148	1.75	0.3153	1.56	1734.3	14.4	1751.9	14.7	1766.8	24.1	99
12	129	126	57	0.97	0.1090	0.46	4.7339	1.57	0.3149	1.50	1783.5	8.4	1773.3	13.3	1764.6	23.2	100
13	46	35	19	0.75	0.1099	0.81	4.6786	1.70	0.3088	1.50	1797.7	14.6	1763.4	14.4	1734.6	22.9	98
14	77	67	34	0.87	0.1084	0.55	4.8387	1.60	0.3237	1.50	1772.7	10.1	1791.7	13.6	1807.9	23.7	99
15	44	41	19	0.94	0.1078	0.63	4.6581	1.66	0.3133	1.54	1763.1	11.5	1759.8	14.0	1756.9	23.7	100
16	50	43	22	0.86	0.1086	0.57	4.7896	1.62	0.3197	1.51	1776.7	10.4	1783.1	13.7	1788.5	23.6	100
17	25	15	10	0.62	0.1091	0.78	4.7589	1.71	0.3163	1.53	1785.0	14.1	1777.7	14.5	1771.5	23.7	100

Table 1 (*continued*)

| Sample	Contents (ppm)				Isotopic ratios								Isotopic ages (Ma)							
Spot	U	Th	Pb	Th/U	$\frac{^{207}Pb}{^{206}Pb}$	±σ	$\frac{^{207}Pb}{^{235}U}$	±σ	$\frac{^{206}Pb}{^{238}U}$	±σ	$\frac{^{207}Pb}{^{206}Pb}$	±σ	$\frac{^{207}Pb}{^{235}U}$	±σ	$\frac{^{206}Pb}{^{238}U}$	±σ	Concor
	ppm	ppm	ppm			%		%		%								%
18	39	29	16	0.74	0.1095	0.98	4.8097	1.79	0.3187	1.50	1790.3	17.8	1786.6	15.2	1783.4	23.4	100
19	39	26	16	0.66	0.1098	0.62	4.8044	1.65	0.3174	1.53	1795.6	11.3	1785.7	14.0	1777.1	23.8	100
20	47	42	20	0.90	0.1086	0.60	4.7140	1.61	0.3147	1.50	1776.8	10.9	1769.7	13.6	1763.7	23.2	100
21	37	31	16	0.84	0.1095	0.67	4.8179	1.76	0.3192	1.63	1790.7	12.2	1788.0	14.9	1785.7	25.5	100
22	53	44	23	0.83	0.1094	0.56	4.8173	1.60	0.3194	1.50	1789.2	10.1	1787.9	13.6	1786.8	23.6	100
23	51	35	21	0.69	0.1086	0.56	4.7916	1.64	0.3200	1.54	1776.3	10.1	1783.4	13.8	1789.5	24.1	100
24	42	31	18	0.74	0.1090	0.60	4.7722	1.63	0.3175	1.51	1783.2	10.9	1780.0	13.8	1777.3	23.6	100
25	42	39	18	0.93	0.1088	0.67	4.7368	1.64	0.3157	1.50	1780.0	12.1	1773.8	13.9	1768.5	23.2	100
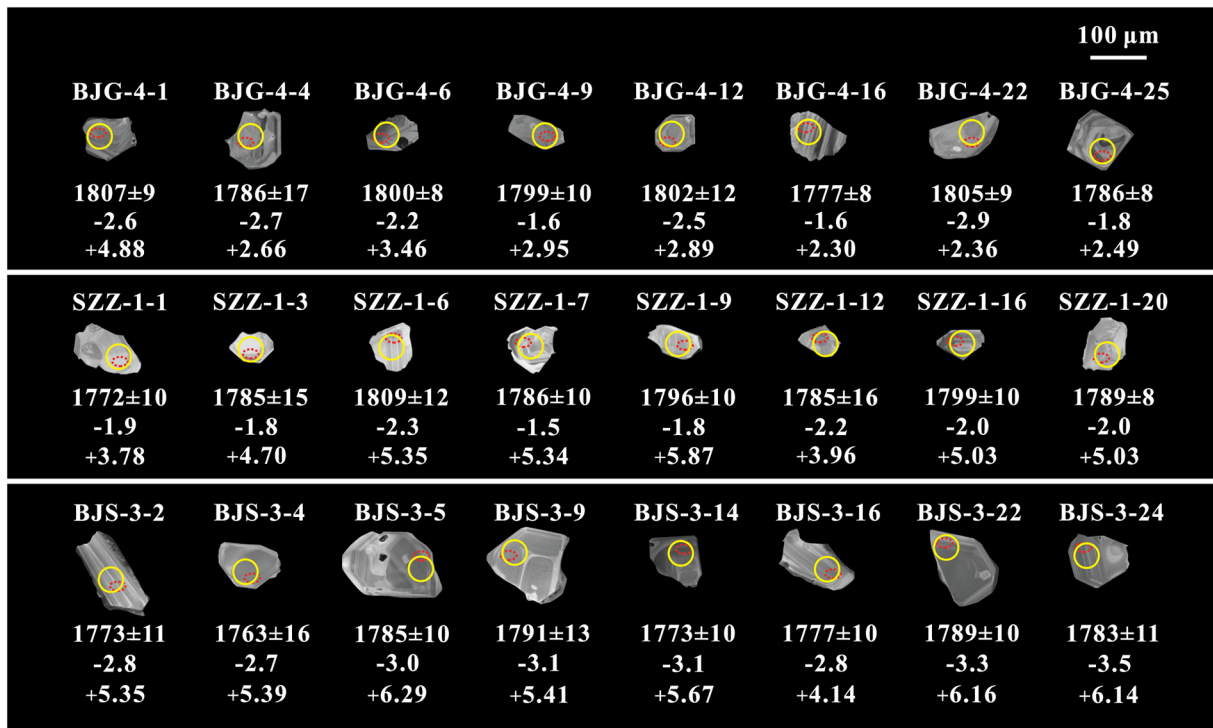
Fig. 6. Cathodoluminescence (CL) images of representative zircons from the Baijiagou, Shizuizi, and Baojiashan rhyolites. Red circles indicate the SIMS analysis spots, and yellow circles denote the MC-ICP-MS analysis spot. The numbers below zircons are $^{207}Pb/^{206}Pb$ ages, $\varepsilon_{Hf}(t)$, and $\delta^{18}O$ values, respectively.
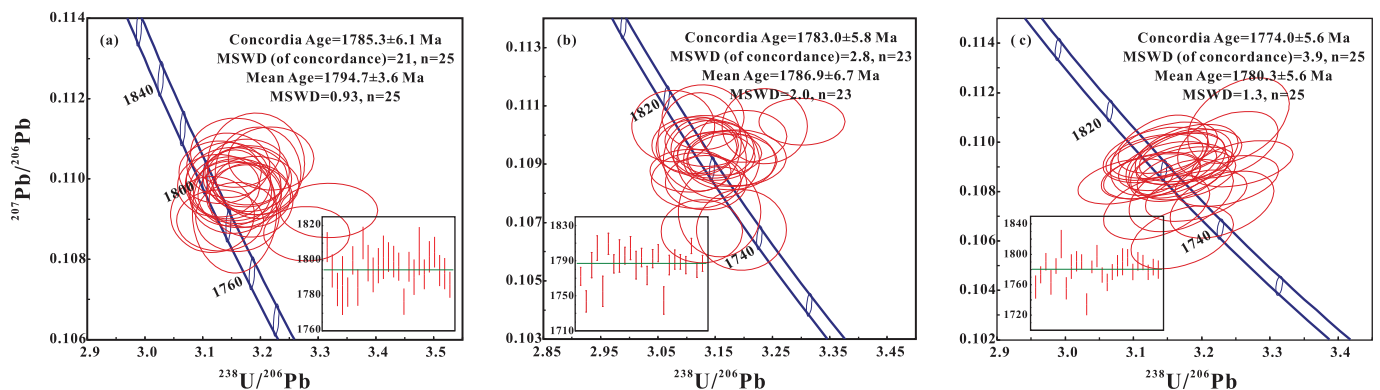

Fig. 7. SIMS zircon U—Pb concordia plots of the Baijiagou (a), Shizuizi (b), and Baojiashan (c) rhyolites.

Table 2
Major and trace element data of Baijiagou, Shizuizi and Baojiashan rhyolites.

Sample	Baijiagou rhyolite				Shizuizi rhyolite			Baojiashan rhyolite					
	BJG-1	BJG-2	BJG-3	BJG-4	SZZ-1	SZZ-2	SZZ-3	BJS-1	BJS-2	BJS-3	BJS-4	BJS-5	BJS-6
SiO_2	71.69	68.96	72.98	68.86	74.38	67.59	68.76	70.09	68.14	69.49	71.78	71.56	70.69
TiO_2	0.56	0.59	0.48	0.53	0.43	0.40	0.65	0.59	0.53	0.52	0.49	0.51	0.53
Al_2O_3	12.27	12.65	7.61	11.54	11.08	13.74	12.44	12.12	12.60	12.48	12.10	12.04	12.36
$Fe_2O_3^T$	5.44	6.93	8.06	7.20	5.04	5.21	7.39	6.07	5.68	6.14	4.70	5.60	5.97
MnO	0.08	0.09	0.18	0.07	0.07	0.10	0.09	0.08	0.09	0.11	0.10	0.07	0.07
MgO	0.24	0.77	1.10	0.25	0.09	0.05	0.51	0.61	1.17	1.08	0.89	0.24	0.44
CaO	0.30	0.39	2.58	1.63	0.19	0.47	0.40	0.24	0.75	0.56	0.20	0.25	0.21
Na_2O	2.59	3.14	1.82	3.01	1.04	0.82	1.82	1.03	1.76	1.78	1.87	1.98	1.36
K_2O	5.96	5.43	1.86	5.24	7.19	10.30	5.89	7.99	6.40	6.12	5.99	6.50	7.00
P_2O_5	0.13	0.12	0.10	0.11	0.07	0.06	0.16	0.12	0.08	0.09	0.08	0.08	0.08
L.O·I	0.46	0.92	2.88	1.51	0.32	0.30	1.26	1.03	2.03	1.77	1.41	0.86	1.15
Total	99.95	100.19	99.71	100.14	100.18	99.32	99.62	100.26	99.36	100.26	99.79	99.87	100.05
$K_2O + Na_2O$	8.55	8.57	3.68	8.25	8.23	11.12	7.71	9.02	8.16	7.90	7.86	8.48	8.36
K_2O/Na_2O	2.30	1.73	1.02	1.74	6.91	12.56	3.24	7.76	3.64	3.44	3.20	3.28	5.15
FeO^T	4.89	6.24	7.25	6.48	4.53	4.69	6.65	5.46	5.11	5.52	4.23	5.04	5.37
A/NK	1.15	1.15	1.52	1.09	1.17	1.10	1.33	1.17	1.28	1.31	1.27	1.17	1.26
A/CNK	1.09	1.08	0.78	0.85	1.13	1.03	1.23	1.12	1.13	1.18	1.22	1.12	1.21
Mg#	9.32	20.6	24.1	7.49	4.00	2.19	13.9	19.0	32.4	29.1	30.6	9.08	14.7
Fe#	0.95	0.89	0.87	0.96	0.98	0.99	0.93	0.90	0.81	0.84	0.83	0.95	0.92
V	15.0	31.0	9.00	17.0	14.0	13.0	17.0	9.00	7.00	5.00	7.00	5.00	11.0
Cr	30.0	30.0	40.0	70.0	40.0	60.0	40.0	30.0	40.0	40.0	20.0	20.0	80.0
Ga	18.8	20.9	15.2	16.9	15.5	16.9	25.0	20.2	25.5	26.6	23.4	17.3	21.4
Rb	200	136	44	139	181	213	166	187	130	142	149	155	200
Sr	62.2	56.7	40.7	55.3	71.9	76.5	48.7	77.1	26.2	30.9	52.1	35.3	46.1
Y	57.3	88.4	64.4	68.4	70.8	81.5	65.9	76.7	73.0	92.5	81.2	76.7	82.4
Zr	590	626	528	589	632	625	642	724	830	811	756	789	827
Nb	25.5	27.1	22.5	25.2	25.7	24.6	21.6	31.0	36.0	34.7	33.1	33.5	34.0
Cs	0.82	0.31	0.23	0.22	2.10	0.94	1.05	0.39	1.35	0.57	0.67	0.76	1.71
Ba	1995	1710	376	1575	2440	2440	2190	2500	1085	1225	1600	1455	1545
La	114	241	109	96.2	105	105	104	139	132	178	165	214	87.3
Ce	241	438	209	182	197	201	189	252	202	319	306	373	177
Pr	27.6	53.7	25.9	22.7	25.2	25.1	24.7	31.1	31.4	41.2	40.2	51.1	22.0
Nd	98.0	195	101	85.7	93.4	91.7	92.6	117	119	154	154	192	82.5
Sm	16.3	34.0	18.5	16.3	19.5	17.9	18.2	20.5	22.6	27.5	29.2	33.9	15.2
Eu	2.45	4.30	2.61	2.25	2.37	2.35	2.26	3.36	4.09	4.33	4.47	4.81	2.24
Gd	12.5	24.1	13.8	13.2	14.2	14.4	13.6	15.5	17.7	20.4	21.7	23.0	13.1
Tb	1.83	3.33	2.12	2.05	2.22	2.49	2.08	2.63	2.91	3.16	3.14	3.06	2.36
Dy	10.5	17.6	12.2	12.2	13.1	14.9	13.1	15.1	15.8	17.8	16.7	15.6	15.8
Ho	2.04	3.17	2.32	2.39	2.69	3.03	2.48	2.95	2.83	3.44	3.08	2.84	3.26
Er	6.68	9.66	7.40	7.59	8.51	9.69	7.50	9.10	8.41	10.4	8.54	8.51	10.1
Tm	0.94	1.35	1.03	1.20	1.26	1.52	1.08	1.40	1.26	1.47	1.25	1.26	1.66
Yb	6.82	8.04	7.06	7.52	8.62	9.33	6.53	8.97	8.13	9.50	8.49	8.50	10.2
Lu	0.95	1.18	1.03	1.13	1.29	1.38	1.03	1.37	1.18	1.42	1.26	1.22	1.52
Hf	15.1	16.4	13.8	15.4	16.0	15.5	15.7	18.8	20.3	21.2	18.9	19.0	20.2
Ta	1.50	1.50	1.20	1.40	1.60	1.40	1.10	1.70	1.80	1.90	1.90	1.70	1.70
Th	20.0	20.1	17.3	17.8	15.2	14.9	13.7	17.1	14.7	14.2	14.4	13.5	13.9
U	3.66	4.67	3.06	3.58	4.24	2.44	2.27	3.56	2.23	2.45	2.42	2.50	2.83
Sn	4.00	5.00	4.00	8.00	4.00	4.00	3.00	4.00	5.00	2.00	2.00	3.00	3.00
W	1.00	2.00	1.00	1.00	3.00	1.00	1.00	4.00	1.00	1.00	1.00	2.00	2.00
∑REE	542	1034	512	452	494	499	478	620	569	791	763	933	444
$(La/Yb)cn$	2.31	3.10	1.96	2.74	3.22	4.17	1.98	2.89	2.20	2.57	2.34	3.14	3.09
δEu	0.53	0.46	0.50	0.47	0.44	0.45	0.44	0.58	0.63	0.56	0.54	0.53	0.49
T_{Zr}	920	919	873	881	937	912	941	945	959	964	963	957	972
10,000Ga/Al	2.89	3.12	3.77	2.77	2.64	2.32	3.80	3.15	3.82	4.03	3.65	2.71	3.27
Zr + Nb + Ce + Y	914	1180	824	864	926	932	919	1084	1141	1257	1176	1272	1120

being spiked with ^{150}Nd and ^{149}Sm tracers. Sm and Nd were separated by conventional ion exchange procedures. Nd isotopic fractionation was corrected to $^{146}Nd/^{144}Nd = 0.721900$, $\lambda^{147}Sm = 6.54 \times 10^{-12}/yr$, with an analytical uncertainty of <3%.

5. Results

5.1. Zircon U—Pb ages

Zircon SIMS U—Pb dating results for the rhyolites are presented in Table 1.

The morphology and geochemistry characteristics of zircons from the three samples are similar. The zircons are generally pale-grey color, subhedral to anhedral, stubby to trigonal, 50 to 150 μm long with length-to-width ratios of 1:1–2:1. They commonly show a weak internal parallel zonation (Fig. 6) and have high Th/U ratios of 0.59 to 0.93 (Table 1), typical features of igneous origin.

Sample BJG-4 (34°56′32.00″ N, 106°40′54.95″ E) is from the Baijiagou region. Twenty-five analyses on 25 grains yield a well-constrained concordia age of 1785.3 ± 6.1 Ma (MSWD of concordance = 21). The $^{207}Pb/^{206}Pb$ ages range from 1777 Ma to 1810 Ma and yield a weighted mean $^{207}Pb/^{206}Pb$ age of 1794.7 ± 3.6 Ma (MSWD = 0.93) (Fig. 7a). The concordia age slightly deviates from the concordia curve, and the value of MSWD of concordance is somewhat high due to the weak lead loss, we thus suggest that the age of 1794.7 ± 3.6 Ma is represented as the crystallization age of the Baijiagou rhyolite.

Twenty-five spots of zircons from sample SZZ-1 (35°21′04.61″ N, 106°26′15.66″ E) in the Shizuizi region were analyzed. Two spots
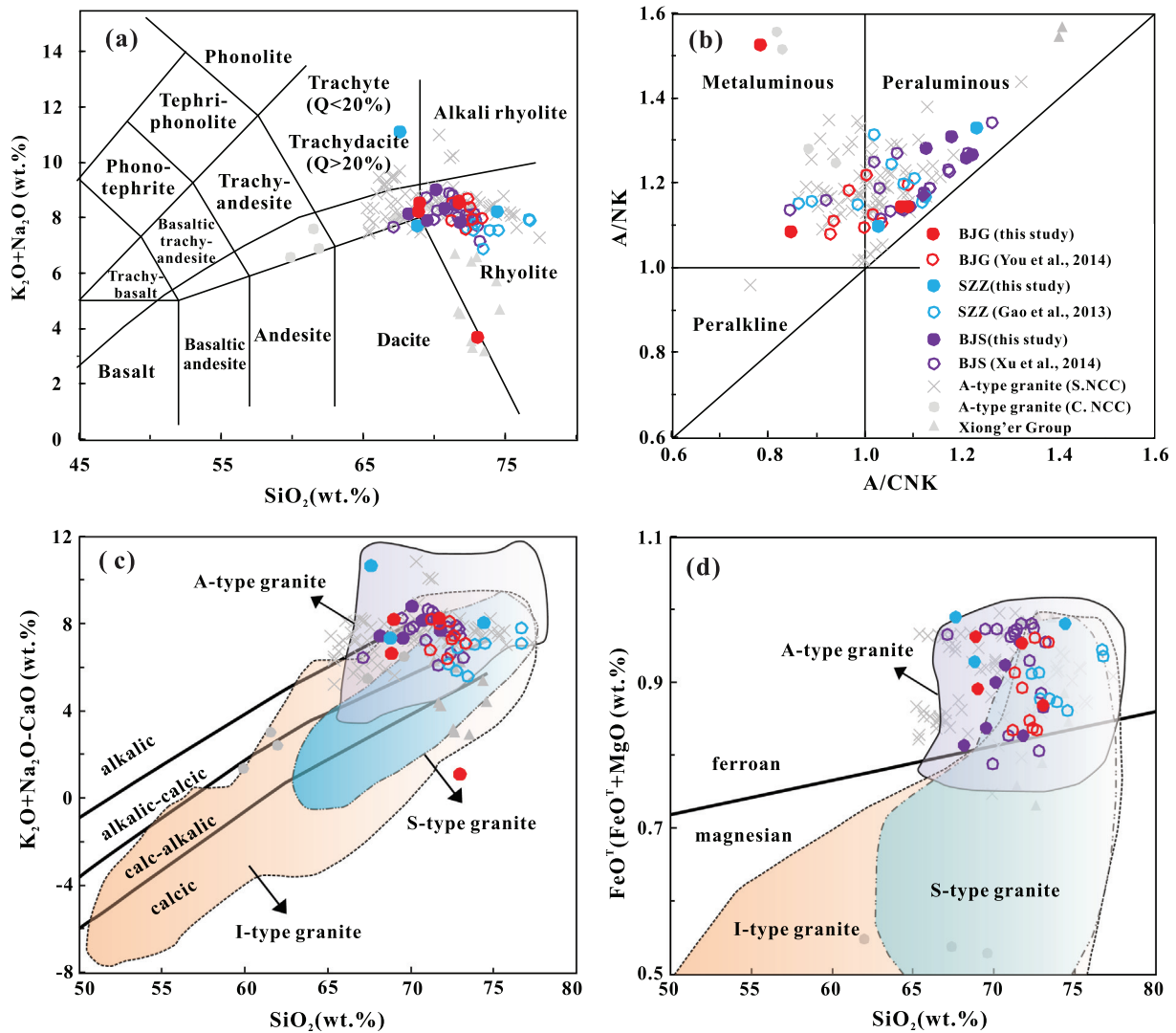
Fig. 8. Major-element geochemical plots for the Baijiagou, Shizuizi and Baojiashan rhyolites: (a) Na$_2$O + K$_2$O vs. SiO$_2$ (wt%) (after Wilson, 1989); (b) A/NK vs. A/CNK (after Maniar and Piccoli, 1989); (c) K$_2$O + Na$_2$O - CaO (wt%) and (d) FeO^T/(FeO^T + MgO) vs. SiO$_2$ (wt%) (after Frost et al., 2001). Data source: previous data of Baijiagou rhyolite from You et al. (2014); previous data of Shizuizi rhyolite from Gao et al. (2013); previous data of Baojiashan rhyolite from Xu et al. (2014); A-type granite in south NCC from Zhao and Zhou (2009), Cui et al. (2013), Shi et al. (2017), Xue et al. (2018) and Deng et al. (2016); A-type granite in central NCC from Geng et al. (2004); acidic rock of Xiong'er Group from Wang et al. (2010).

(SZZ-1-10 and SZZ-1-22) with large errors are excluded for further calculation. The remaining 23 analyses are located on the concordia curve and yield a concordia age of 1783.0 ± 5.8 Ma (MSWD of concordance = 2.8). The ^{207}Pb/^{206}Pb ages ranging from 1777 Ma to 1810 Ma, and generate a weighted mean ^{207}Pb/^{206}Pb age of 1786.9 ± 6.7 Ma (MSWD = 2.0) (Fig. 7b). We prefer the weighted mean age of 1786.9 ± 6.7 Ma as the crystallization age of the Shizuizi rhyolite.

Sample BJS-3 (35°03′39.49″ N, 106°34′27.19″ E) is from the Baojiashan region. Twenty-five analyzed spots of zircons were located on the concordia curve with ^{207}Pb/^{206}Pb age ranges from 1777 Ma to 1810 Ma, and yield a concordia age and a weighted mean ^{207}Pb/^{206}Pb age of 1774.0 ± 5.6 Ma (MSWD of concordance = 3.9) and 1780.3 ± 5.6 Ma (MSWD = 1.3) (Fig. 7c), respectively. We suggest that the age of 1780.3 ± 5.6 Ma is interpreted as the emplacement age of the Baojiashan rhyolite.

5.2. Whole-rock major and trace element compositions

Both major and trace element data are listed in Table 2. Rocks from the three regions show similar chemical compositions. They have high SiO$_2$ (67.59 to 74.38 wt%), K$_2$O (1.86 to 10.30 wt%), and Na$_2$O (1.03 to 3.14 wt%), and low MnO (0.07–0.18 wt%), CaO (0.19–2.58 wt%), TiO$_2$

(0.40–0.65 wt%) and P$_2$O$_5$ (0.08–0.16 wt%), and thus all samples are plotted within the sub-alkaline rhyolite (Fig. 8a) and alkalic-calcic fields (Fig. 8c). Their A/CNK and A/NK ratios range from 0.85 to 1.22 and 1.09 to 1.33, respectively (Fig. 8b). All samples have low MgO (0.05–1.17 wt%), low Mg# (100 × MgO/(MgO + FeO^T) = 2.19–32.4) and high Fe# (FeO^T/(FeO^T + MgO) = 0.81–0.99), showing affinities of ferroan granites/rhyolites (Fig. 8d). In the Harker diagrams, TiO$_2$, Al$_2$O$_3$, P$_2$O$_5$, and Fe$_2$O$_3^T$ are negatively correlated with SiO$_2$ (Fig. 9a-d).

All these samples show similar chondrite-normalized REE patterns, which are rich in LREE ((La/Yb)$_N$ = 6.17–21.5) and display pronounced negative Eu anomalies (Eu/Eu* = 0.44–0.63) (Fig. 10a). Their total REE contents vary from 444 ppm to 1034 ppm. In the primitive mantle normalized spider diagram, they show negative Nb, Ta, Sr, P and Ti anomalies (Fig. 10b). They have high Rb (43.9–200 ppm), Ga (15.2–26.6 ppm), Zr (528–830 ppm), Ce (177–438 ppm), and Y (57.3–92.5 ppm) concentrations.

5.3. Whole-rock Sm—Nd compositions

Two representative samples from each rhyolite unit were selected for whole-rock Sm—Nd isotopic analysis (Table 3). The samples from different rhyolites show similar Sm—Nd isotopic characteristics. They
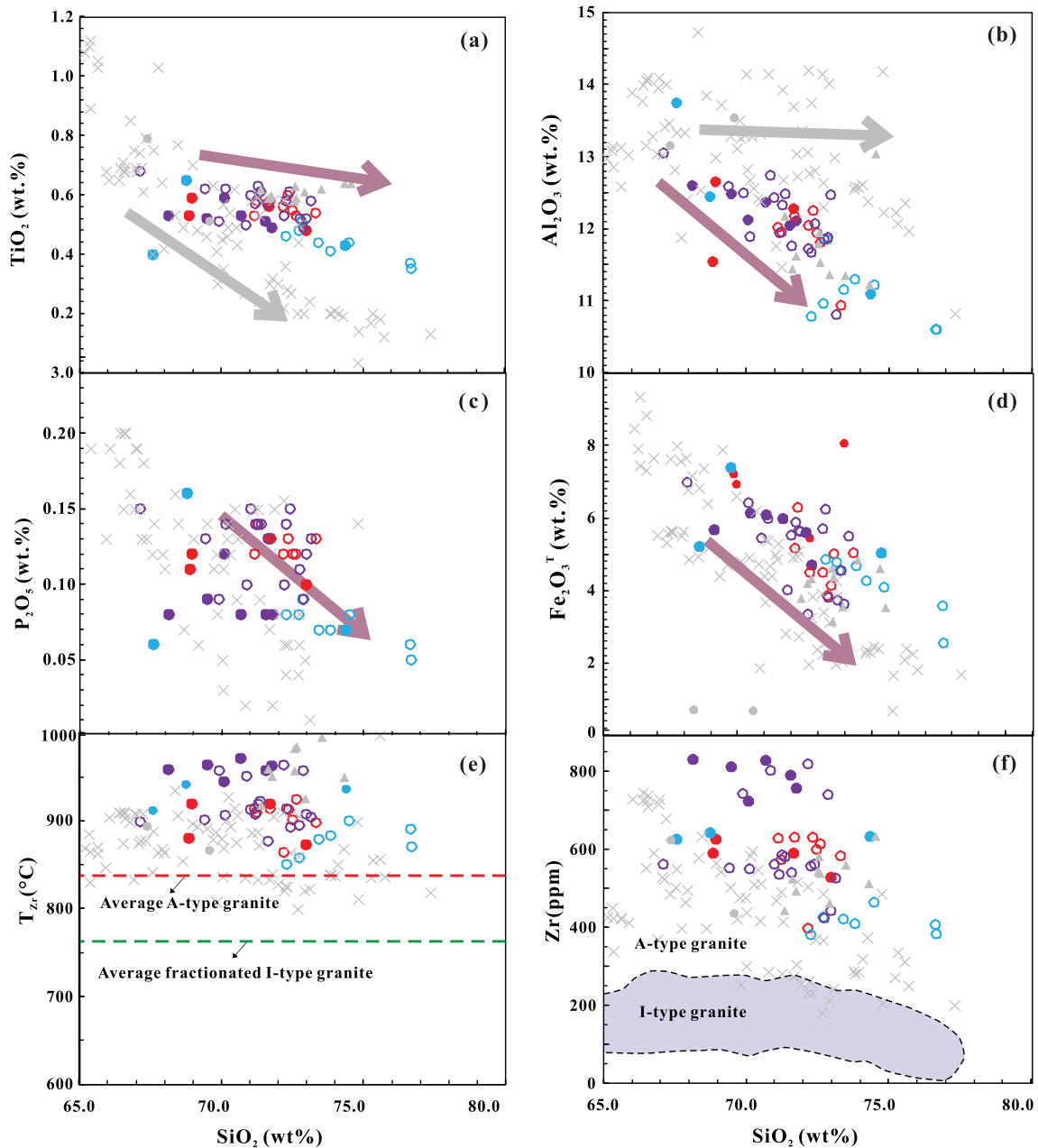
Fig. 9. Harker plots of major and trace elements of the Baijiagou, Shizuizi, and Baojiashan rhyolites. (a-d) TiO_2, Al_2O_3, CaO and $Fe_2O_3^T$ vs. SiO_2 (wt%); (e) T_{Zr} (°C) vs. SiO_2 (wt%), T_{Zr} (°C): the calculated Zr saturation temperatures (Watson and Harrison, 1983); average A-type granite and fractionated I-type granite from King et al. (1997); (f) Zr (ppm) vs. SiO_2 (wt%) (after King et al., 2001). Symbols as in Fig. 8.

have $^{147}Sm/^{144}Nd$ ratios of 0.1056–0.1188 and $^{143}Nd/^{144}Nd$ ratios of 0.511299–0.511554, corresponding to $\varepsilon_{Nd}(t)$ values of −5.87 to −3.31 with Neoarchean two-stage model ages (T_{DM}^C) of 2.54–2.74 Ga. (Fig. 11a).

5.4. Zircon Hf—O isotopic compositions

Three samples (BJG-4, SZZ-1, and BJG-3) were further analyzed for the Hf—O isotopes with results listed in Table 4. Initial $^{176}Hf/^{177}Hf$ ratios were calculated using their in-situ U—Pb zircon ages.

Zircons from three rhyolites display similar zircon Lu—Hf isotopic composition. They show low $^{176}Lu/^{177}Hf$ ratios (0.000466 to 0.001188), a narrow range of initial $^{176}Hf/^{177}Hf$ ratios (0.281558 to 0.281626) and $\varepsilon_{Hf}(t)$ values (−3.6 to −1.5) with two-stage Hf model

ages of 2.57–2.70 Ga (Fig. 11b). However, their $\delta^{18}O$ values are slightly different. The $\delta^{18}O$ values increase from 1.5–5.3‰ in Baijiagou sample (BJG-4), through 3.3–5.9‰ in Shizuizi sample (SZZ-1), to 4.1–6.8‰ in Baojiashan sample (BJS-3) (Fig. 12).

6. Discussion

6.1. Aluminous A-type rhyolites

The petrographic characteristics show that the felsic rocks from the three regions have the unique characteristics of volcanic lava, such as porphyry, rhyolitic structure (flow banding), vesicular and amygdaloidal texture of rocks, autoclastic texture, melting corrosion structure, fiber structure of mineral grains, as well as felsitic and spherulitic

11
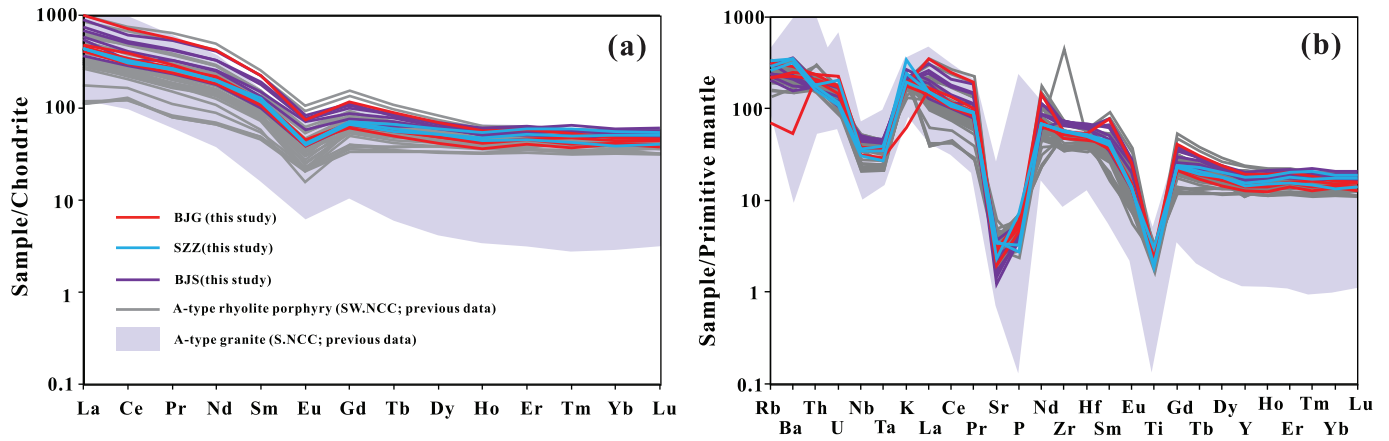
Fig. 10. Chondrite-normalized REE patterns (a) and primitive-mantle normalized trace element spider diagrams (b) for the Baijiagou, Shizuizi, and Baojiashan rhyolites. The normalization values are from Sun and McDonough (1989). Data source: previous data of A-type rhyolites in southwest NCC from You et al. (2014), Gao et al. (2013) and Xu et al. (2014); A-type granite in south NCC from Zhao and Zhou (2009), Cui et al. (2013), Shi et al. (2017), Xue et al. (2018) and Deng et al. (2016).

Table 3
Whole-rock Sm—Nd isotopic composition of the Baijiagou, Shizuizi and Baojiashan rhyolites.

Sample	Age(Ma)	Sm(ppm)	Nd(ppm)	$^{147}Sm/^{144}Nd$	$^{143}Nd/^{144}Nd$	2σ	$\varepsilon_{Nd}(t)$	T_{DM} (Ma)	T^C_{DM}(Ma)
BJG-2	1795	34.0	195	0.10564872	0.511327	0.000004	−4.62	2558	2656
BJG-3	1795	18.5	101	0.11040339	0.511351	0.000005	−5.25	2640	2707
SZZ-2	1786	17.9	91.7	0.11797925	0.511493	0.000005	−4.31	2624	2624
SZZ-3	1786	18.2	92.6	0.11879238	0.511554	0.000005	−3.31	2550	2544
BJS-3	1780	27.5	154	0.10792301	0.511299	0.000004	−5.87	2653	2744
BJS-4	1780	27.5	154	0.10792517	0.511384	0.000004	−4.20	2532	2611

texture of matrix. In addition, there are many apatite inclusions in zircon. These specialized structures and textures correspond to the pressure drop and rapid cooling in the process of magma crystallization, indicating that the rocks belong to extrusive facies and should be named by rhyolites rather than granites as previously thought (Gao et al., 2013; Xu et al., 2014; You et al., 2014).

The rhyolite samples from three regions are metaluminous to peraluminous, and some samples are strong peraluminous (A/CNK = 0.85–1.22), similar to those of S-type granites. They have low P_2O_5 content (0.06–0.16 wt%, 0.10 wt% on average) that is negatively correlated with SiO_2 (Fig. 9c). Moreover, no aluminum-rich minerals, such as

muscovite, cordierite, and garnet, have been found in the samples. These features are different from those of S-type granite (Chappell, 1999).

Strong felsic A-type granites ($SiO_2 > 72$ wt%) have chemical and mineralogical characteristics similar to those highly fractionated I-type granite (King et al., 1997). A-type granite has higher FeO^T (>1.00 wt%) than high-fractionated I-type granite (<1.00 wt%). Moreover, A-type granite has low Rb content (<270 ppm) and high Ba, Sr, Zr + Nb + Ce + Y and Ga/Al ratio (Whalen et al., 1987). In addition, magma temperatures (>800 °C) of A-type granite are generally higher than high-fractionated I-type granite. The rhyolite samples in this study have low Rb
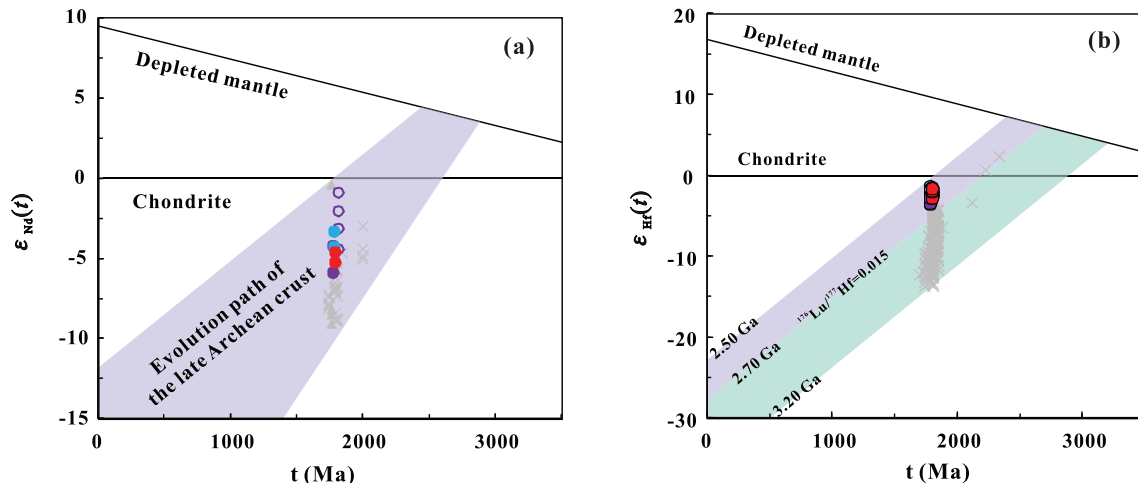

Fig. 11. Diagram of $\varepsilon_{Nd}(t)$ vs. age (a) and $\varepsilon_{Hf}(t)$ vs. age (b) for samples of the Baijiagou, Shizuizi, and Baojiashan rhyolites. Symbols as in Fig. 8.

Table 4
Lu—Hf isotope compositions and O isotope data of zircons from the Baijiagou, Shizuizi and Baojiashan rhyolites.

Sample No.	t (Ma)	$^{176}Yb/^{177}Hf$	$^{176}Lu/^{177}Hf$	$^{176}Hf/^{177}Hf$	2σ	$\varepsilon_{Hf}(t)$	T_{DM}	T_{DM}^{C}	$f_{Lu/Hf}$	$\delta^{18}O$	±2σ
Sample BJG-4											
1	1795	0.019216	0.000559	0.281574	0.000015	−2.6	2306	2647	−0.98	4.88	0.25
2	1795	0.018275	0.000540	0.281584	0.000017	−2.3	2292	2624	−0.98	4.92	0.10
3	1795	0.018305	0.000533	0.281587	0.000016	−2.2	2287	2617	−0.98	3.26	0.24
4	1795	0.017050	0.000494	0.281570	0.000015	−2.7	2308	2652	−0.99	2.66	0.36
5	1795	0.018273	0.000529	0.281580	0.000017	−2.4	2297	2633	−0.98	4.37	0.17
6	1795	0.019825	0.000559	0.281588	0.000017	−2.2	2287	2616	−0.98	3.46	0.29
7	1795	0.020796	0.000572	0.281586	0.000016	−2.3	2291	2622	−0.98	3.57	0.21
8	1795	0.016586	0.000483	0.281577	0.000017	−2.5	2298	2635	−0.99	2.38	0.24
9	1795	0.016757	0.000488	0.281600	0.000018	−1.6	2267	2583	−0.99	2.95	0.30
10	1795	0.016528	0.000482	0.281571	0.000015	−2.7	2306	2648	−0.99	4.49	0.17
11	1795	0.017608	0.000511	0.281566	0.000017	−2.9	2314	2661	−0.98	1.58	0.31
12	1795	0.028442	0.000797	0.281587	0.000016	−2.5	2302	2636	−0.98	2.89	0.41
13	1795	0.020432	0.000593	0.281577	0.000016	−2.6	2305	2644	−0.98	5.25	0.14
14	1795	0.022124	0.000635	0.281580	0.000016	−2.5	2303	2640	−0.98	1.47	0.27
15	1795	0.022274	0.000644	0.281587	0.000018	−2.3	2294	2625	−0.98	4.36	0.15
16	1795	0.022177	0.000635	0.281606	0.000018	−1.6	2268	2581	−0.98	2.30	0.24
17	1795	0.018715	0.000543	0.281573	0.000016	−2.7	2306	2648	−0.98	2.55	0.32
18	1795	0.016890	0.000492	0.281585	0.000016	−2.2	2288	2618	−0.99	2.73	0.40
19	1795	0.017228	0.000490	0.281587	0.000016	−2.1	2284	2612	−0.99	2.60	0.20
20	1795	0.018108	0.000524	0.281593	0.000015	−1.9	2278	2601	−0.98	5.04	0.22
21	1795	0.018771	0.000544	0.281595	0.000017	−1.9	2277	2599	−0.98	2.99	0.34
22	1795	0.016202	0.000472	0.281563	0.000015	−2.9	2316	2665	−0.99	2.36	0.27
23	1795	0.016029	0.000466	0.281586	0.000017	−2.1	2285	2614	−0.99	2.40	0.31
24	1795	0.017057	0.000498	0.281591	0.000017	−2.0	2280	2605	−0.98	3.75	0.22
25	1795	0.028679	0.000809	0.281607	0.000018	−1.8	2277	2593	−0.98	2.49	0.32
Sample SZZ-1											
1	1786	0.036954	0.001030	0.281617	0.000018	−1.9	2275	2592	−0.97	3.78	0.31
2	1786	0.025955	0.000753	0.281606	0.000018	−1.9	2274	2595	−0.98	4.31	0.30
3	1786	0.021562	0.000627	0.281605	0.000018	−1.8	2268	2588	−0.98	4.70	0.17
4	1786	0.033168	0.000939	0.281614	0.000017	−1.9	2275	2592	−0.97	4.23	0.23
5	1786	0.023746	0.000696	0.281599	0.000017	−2.1	2281	2607	−0.98	5.85	0.13
6	1786	0.016985	0.000504	0.281588	0.000016	−2.3	2285	2618	−0.98	5.35	0.20
7	1786	0.033570	0.000956	0.281626	0.000017	−1.5	2259	2566	−0.97	5.34	0.21
8	1786	0.024855	0.000723	0.281602	0.000017	−2.0	2278	2602	−0.98	5.08	0.18
9	1786	0.035922	0.001003	0.281618	0.000017	−1.8	2273	2588	−0.97	5.87	0.19
10	1786	0.029408	0.000837	0.281616	0.000016	−1.7	2266	2580	−0.97	3.62	0.20
11	1786	0.024221	0.000703	0.281616	0.000019	−1.5	2258	2569	−0.98	3.64	0.30
12	1786	0.019624	0.000577	0.281594	0.000021	−2.2	2280	2609	−0.98	3.96	0.31
13	1786	0.019184	0.000556	0.281582	0.000018	−2.6	2296	2636	−0.98	3.33	0.40
14	1786	0.039016	0.001094	0.281618	0.000020	−1.9	2279	2596	−0.97	5.00	0.26
15	1786	0.028020	0.000804	0.281611	0.000018	−1.8	2270	2588	−0.98	4.85	0.18
16	1786	0.020600	0.000599	0.281599	0.000018	−2.0	2275	2601	−0.98	5.03	0.23
17	1786	0.039439	0.001100	0.281620	0.000019	−1.9	2276	2592	−0.97	3.81	0.23
18	1786	0.023671	0.000686	0.281605	0.000017	−1.9	2272	2593	−0.98	3.37	0.37
19	1786	0.019139	0.000567	0.281600	0.000016	−2.0	2272	2596	−0.98	5.17	0.28
20	1786	0.019890	0.000585	0.281600	0.000017	−2.0	2273	2597	−0.98	5.03	0.31
21	1786	na	na	na	na	na	na	na	na	3.43	0.33
22	1786	na	na	na	na	na	na	na	na	3.99	0.17
23	1786	na	na	na	na	na	na	na	na	3.99	0.26
24	1786	na	na	na	na	na	na	na	na	5.94	0.20
25	1786	na	na	na	na	na	na	na	na	5.08	0.20
Sample BJS-3											
1	1780	0.022811	0.000635	0.281576	0.000018	−3.0	2308	2658	−0.98	6.79	0.17
2	1780	0.037439	0.001013	0.281595	0.000018	−2.8	2305	2645	−0.97	5.35	0.16
3	1780	0.022432	0.000628	0.281558	0.000017	−3.6	2332	2698	−0.98	4.66	0.23
4	1780	0.038039	0.001026	0.281598	0.000017	−2.7	2302	2640	−0.97	5.39	0.15
5	1780	0.032593	0.000879	0.281585	0.000017	−3.0	2311	2657	−0.97	6.29	0.22
6	1780	0.034306	0.000932	0.281596	0.000017	−2.6	2298	2635	−0.97	6.33	0.13
7	1780	0.031567	0.000858	0.281580	0.000018	−3.1	2317	2667	−0.97	5.58	0.22
8	1780	0.026588	0.000736	0.281580	0.000018	−3.0	2309	2658	−0.98	5.04	0.21
9	1780	0.023303	0.000656	0.281573	0.000017	−3.1	2314	2667	−0.98	5.41	0.29
10	1780	0.029401	0.000800	0.281580	0.000017	−3.1	2313	2663	−0.98	5.92	0.10
11	1780	0.037749	0.001020	0.281588	0.000019	−3.1	2315	2661	−0.97	5.61	0.16
12	1780	0.045579	0.001188	0.281597	0.000015	−2.9	2313	2653	−0.96	6.29	0.16
13	1780	0.031326	0.000864	0.281573	0.000017	−3.4	2326	2682	−0.97	6.56	0.17
14	1780	0.022680	0.000633	0.281573	0.000015	−3.1	2312	2665	−0.98	5.67	0.17
15	1780	0.023944	0.000660	0.281577	0.000017	−3.0	2308	2658	−0.98	6.12	0.19
16	1780	0.035048	0.000935	0.281592	0.000019	−2.8	2305	2646	−0.97	4.14	0.19
17	1780	0.025094	0.000706	0.281574	0.000017	−3.2	2315	2668	−0.98	6.06	0.16
18	1780	0.029910	0.000820	0.281573	0.000016	−3.3	2324	2679	−0.98	6.07	0.11
19	1780	0.020874	0.000587	0.281567	0.000016	−3.3	2318	2676	−0.98	5.94	0.17
20	1780	0.030854	0.000839	0.281578	0.000018	−3.2	2318	2670	−0.97	4.30	0.19

Table 4 (*continued*)

Sample No.	t (Ma)	^{176}Yb/^{177}Hf	^{176}Lu/^{177}Hf	^{176}Hf/^{177}Hf	2σ	$\varepsilon_{Hf}(t)$	T_{DM}	T_{DM}^C	$f_{Lu/Hf}$	δ^{18}O	±2σ
21	1780	0.021802	0.000613	0.281564	0.000017	−3.4	2323	2683	−0.98	5.45	0.18
22	1780	0.031172	0.000851	0.281574	0.000017	−3.3	2324	2680	−0.97	6.16	0.19
23	1780	0.020586	0.000571	0.281563	0.000016	−3.4	2321	2682	−0.98	5.81	0.16
24	1780	0.022637	0.000632	0.281563	0.000017	−3.5	2326	2687	−0.98	6.14	0.15
25	1780	0.036662	0.000992	0.281593	0.000019	−2.8	2307	2648	−0.97	4.34	0.21

$\varepsilon_{Hf}(t) = [(^{176}Hf/^{177}Hf)_S - (^{176}Lu/^{177}Hf)_S \times (e^{\lambda t}-1)]/[(^{176}Hf/^{177}Hf)_{CHUR,(0)}\,^{176}Lu/^{177}Hf)_{CHUR} \times (e^{\lambda t}-1)-1] \times 10{,}000$;

$T_{DM1} = 1/\lambda \times \ln[1 + ((^{176}Hf/^{177}Hf)_S - (^{176}Hf/^{177}Hf)_{DM})/((^{176}Lu/^{177}Hf)_S - (^{176}Lu/^{177}Hf)_{DM})]$;

$T_{DM}^C = T_{DM1} - (T_{DM1}-t) \times [(f_{CC}-f_S)/(f_{CC}-f_{DM})]$;

$f_{Lu/Hf} = (^{176}Hf/^{177}Hf)_S/(^{176}Lu/^{177}Hf)_{CHUR}-1$;

f_{CC}, f_S and f_{DM} are the $f_{Lu/Hf}$ values of the mean crust, zircon sample and the depleted mantle;

subscript S = analyzed zircon samples, CHUR = chondritic uniform reservoir; DM = depleted mantle;

$\lambda = 1.867 \times 10^{-11}$ year^{-1}, decay constant of ^{176}Lu;

$(^{176}Hf/^{177}Hf)_{DM} = 0.28325$; $(^{176}Lu/^{177}Hf)_{DM} = 0.0384$; $(^{176}Hf/^{177}Hf)_{CHUR,(0)} = 0.282772$;

$(^{176}Hf/^{177}Hf)_{CHUR} = 0.0332$; $(^{176}Lu/^{177}Hf)_{mean\ crust} = 0.015$.

(43.9–213 ppm), high FeO^T (4.23–7.25 wt%), FeO^T/(FeO^T + MgO) (0.81–0.99), Ba (1085–2440 ppm), Sr (26.2–77.1 ppm), Zr + Nb + Ce + Y (824–1272 ppm) and 10,000 × Ga/Al ratio (2.32–4.03), as well as high Zr contents (528–830 ppm; Fig. 9f) and zirconium saturation temperatures (T_{Zr} = 873–964 °C; Fig. 9e), plotting in the A-type granite field in the discrimination diagrams (Fig. 13).

In addition, the rhyolites are enriched in large ion lithophile elements (LILE) and the high field strength elements (HFSE) and have high Rb/Sr ratios (>2.39). King et al. (1997) proposed that metaluminous to weak peraluminous A-type granite is defined as 'aluminous A-type granites' and should not be grouped with peralkaline granite. Therefore, the rhyolites in this study are classified as aluminous A-type rhyolites.

6.2. Petrogenesis and implication

6.2.1. Partial melting of the Neoarchean felsic basement rocks

Several mechanisms have been proposed for the petrogenesis of A-type granitic rocks, including (1) extreme fractional crystallization of mantle-derived melts (e.g., Shellnutt and Zhou, 2007), (2) partial melting of crustal rocks (e.g., Patiño Douce, 1997), and (3) combination of crustal- and mantle-derived materials, including crustal assimilation and fractional crystallization of mafic magma, or mixing of the two end-members (e.g., Yang et al., 2006).

In general, fractional crystallization of mantle-derived magmas produces peralkaline melts (e.g., King et al., 1997; Patiño Douce, 1997), inconsistent with the metaluminous-peraluminous characteristics of the rhyolites studied in this paper. Their high SiO$_2$ and low Mg$^\#$, Cr, Co, and Ni concentrations indicated no mantle-derived material was involved in the origin. The rhyolite samples also have high Rb/Sr ratios, negative $\varepsilon_{Nd}(t)$ and $\varepsilon_{Hf}(t)$ values (Fig. 11), different from the mantle-derived A-type granites which generally show high and positive Nd—Hf isotopic values (e.g., King et al., 1997; Patiño Douce, 1997). Moreover, the felsic rocks formed by fractional crystallization are usually associated with mafic to intermediate rocks, which is inconsistent with the characteristic of the study area. Therefore, it is unlikely that the rhyolites were formed by fractional crystallization of mantle-derived magmas.

Magma mixing between mantle- and crustal-derived melts has been proposed to produce A-type granites, which generally have a wide range of elemental and isotopic compositions (Griffin et al., 2002). However, our samples display narrow ranges of whole-rock $\varepsilon_{Nd}(t)$ and zircon $\varepsilon_{Hf}(t)$ values without a bimodal distribution (Fig. 11). Besides, mafic microgranular enclaves and acicular apatite representing magma mixing are absent in the rocks, suggesting that magma mixing was not the major mechanism.

The aluminous A-type rhyolites in this study have high SiO$_2$ (>67.59 wt%), low MgO (<1.17 wt%), TiO$_2$ (<0.65 wt%) and FeO^T

(<7.25 wt%) and show enrichment of large ion lithophile elements (Rb, Th, U and K) and depletion of high field strength elements (Nb, Ta, Zr and Hf), and remarkable depletion of Sr and Eu (Fig. 10), typical features of crustal origin. They also have low Th/U (5.4–8.3) and moderate Nb/Ta (15.1–22.4), similar to those of the middle-lower crust (Th/U = 6, Nb/Ta = 16.5; Rudnick and Gao, 2003). In addition, these volcanic rocks fall in the field of the pure crustal partial melts in the discriminant diagram (Fig. 14a; Rapp et al., 1999; Smithies, 2000). Their negative $\varepsilon_{Hf}(t)$ (−3.6 to −1.8) and $\varepsilon_{Nd}(t)$ values (−5.9 to −3.3) are significantly lower than those of the mantle-derived rocks or the juvenile crustal rocks. These lines of evidence, in combination with their Neoarchean two-stage Hf model ages (2.70–2.57 Ga), suggest that the rhyolites were derived from ancient crust.

Potential crustal components of the A-type granite include granulitic metasedimentary rocks (Huang et al., 2011), anhydrous lower crustal granulitic residue from which granitic melts were previously extracted (King et al., 1997; Whalen et al., 1987) and calc-alkaline granitoids in the shallow crust (Creaser et al., 1991; Patiño Douce, 1997).

Magmas derived from granulite facies metasedimentary rocks usually displayed low alkali content, high Al$_2$O$_3$ content, and strong peraluminous affinity. However, the rhyolites in this study have high alkali (3.68–11.12 wt%), low Al$_2$O$_3$ (7.61–13.7 wt%), and are metaluminous to weakly peraluminous (Huang et al., 2011; Sylvester, 1998). Moreover, the product of partial melting of refractory granulitic residues is usually depleted in TiO$_2$ relative to MgO and alkali relative to alumina (Creaser et al., 1991; Patiño Douce, 1997), whereas the rhyolites display high TiO$_2$/MgO (>0.44), (Na$_2$O + K$_2$O)/Al$_2$O$_3$ (>0.48) ratios. In addition, experimental petrology has established that the residual granulite source is too refractory to produce A-type granite melt (Creaser et al., 1991). Hence, the first two possibilities were ruled out. Instead, both the elemental and isotopic data suggest that the rhyolites were derived from the partial melting of the granitic magma source. Their high K$_2$O/Na$_2$O ratios, low CaO and P$_2$O$_5$ contents and depletion in Eu and Sr are similar to those of the experimental melts derived through partial melting of tonalite and granodiorite with a plagioclase-rich residual under high temperatures (Patiño Douce, 1997). Therefore, we propose that the rhyolites are partial melts of calc-alkaline granitoids, yet the specific source cannot be addressed due to the research gap of the basement rocks in the study area.

A-type granites/rhyolites generally were formed under high temperatures than the other felsic rocks (e.g., King et al., 1997; Loiselle and Wones, 1979; Watson and Harrison, 1983). High temperatures are necessary for melting of felsic crustal rocks which have limited H$_2$O availability and relatively low oxygen fugacity for generation of aluminous A-type granites/rhyolites (e.g., King et al., 1997, 2001). The zircon saturation temperatures reveal that the melting occurred above 850 °C, which was initiated by mantle upwelling and crustal

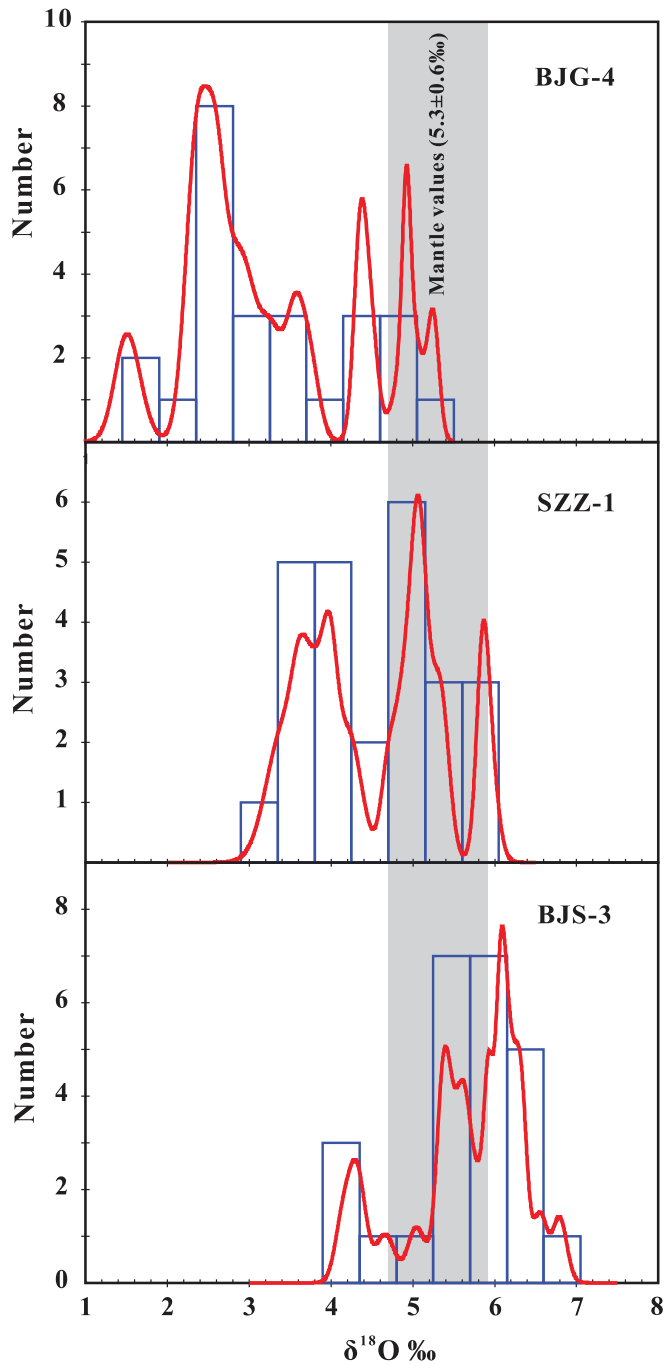**Fig. 12.** Binned frequency histograms of zircon δ^{18}O of the Baijiagou, Shizuizi, and Baojiashan rhyolites.

thinning, possibly through the underplating of mafic magmas (King et al., 1997).

6.2.2. Low δ^{18}O felsic magmatism

The magmatic zircons from the rhyolites show low δ^{18}O values (1.5–6.8‰) (Fig. 12), which is the first identified late Paleoproterozoic low δ^{18}O magmatism in the southwestern margin of the NCC. Zircons crystallized in crustal derived magmas commonly show δ^{18}O values ranging from mantle-like value of 5.3 ± 0.6‰ (2δ; Valley et al., 2005) to 14–16‰ associated with increasing incorporations of supracrustal materials (Bindeman and Valley, 2002; Valley et al., 2005). Low δ^{18}O

igneous rocks are formed by melting of pre-existing ^{18}O-depleted parental rock (pre-magmatic; Zheng et al., 2004), assimilation of high-T hydrothermally altered rocks (*syn*-magmatic; Larson and Geist, 1995), interaction with low δ^{18}O liquids in magma chambers (syn-magmatic; Hildreth et al., 1984) and later high-T water/rock interaction (post-magmatic; Wang et al., 2011; Huang et al., 2019).

In general, zircon is much more resistant than other minerals to diffuse and reset its δ^{18}O values during late hydrothermal alterations (Bindeman and Valley, 2002; Valley, 2003). High-T hydrothermal alteration (700–800 °C) can change zircon oxygen isotopic composition in a reasonable geological time scale (Zheng et al., 2004). Most zircons in this study show normal magmatic zoning textures and trace element compositions (high Th/U ratios of 0.49–1.0), suggesting magmatic origin. Meanwhile, the zircon δ^{18}O values are not correlated with U and Th/U, suggesting late alteration did not change their O isotope compositions. Moreover, these zircons do not show any healed cracks that are generally determined as metamict zircons recrystallized under hydrothermal conditions (Zhang and Zheng, 2011). These lines of evidence rule out the effects of post-magmatic activities on the oxygen isotopes. Thus, the measured zircon δ^{18}O values represent primary oxygen isotopic compositions of the parental magmas (Valley et al., 2005) and low zircon δ^{18}O values could not be ascribed to the post-magmatic alteration.

The influx of low δ^{18}O fluid into a magma chamber or assimilation of ^{18}O-depleted wall rock during magmatic activity could result in strongly heterogeneous O isotope compositions, and their partial melts may have inherited such large variable δ^{18}O characters (Zheng et al., 2004). However, the three series of volcanic rocks show narrow ranges of δ^{18}O values with various units of 3.8‰ to 2.6‰, ruling out the possibility of crustal assimilation. In terms of mineralogical characteristics, inherited zircons are not recognized in the three rhyolites. In addition, they have constant $\varepsilon_{Hf}(t)$ (−3.6 to −1.5), $\varepsilon_{Nd}(t)$ values (−5.87 to −3.31) and $(La/Sm)_N$ ratios, which are not correlated with SiO_2 in Fig. 15, suggesting no significant crustal contamination or magma mixing occurred. In addition, significant interaction between liquid water and magma chamber is impossible on physical grounds (Taylor and Sheppard, 1986).

Based on the above discussions, the low δ^{18}O character of the three series rhyolites was inherited from their parental sources (Neoarchean felsic crustal materials), whose δ^{18}O has been depleted through high-temperature hydrothermal alteration before partial melting. Although no basement rocks with low δ^{18}O have been identified in the region, tour results demonstrate that Neoarchean low δ^{18}O basement rocks were developed in this area.

6.2.3. Implication for the crustal evolution of the southwestern margin of the NCC

The Ordos Block is an important part of the Western Block in the NCC (Fig. 1b). The nature of the basement rocks and the early Precambrian crustal evolution in the Ordos Block are not clear due to limited occurrence of the Precambrian rocks (Zhang et al., 2015). Recently, the early Precambrian basement rocks have been found in some drill holes in the north-central part of the Ordos Block (Zhang et al., 2015). Their zircon U—Pb ages and Lu—Hf isotopes indicate that Neoarchean crustal basement rocks are indeed existed beneath the Ordos Block, which had a major crustal growth at ~2.7 Ga, and subjected to crustal reworking at ~2.5 Ga and widespread granitoid magmatism at 2.2–2.0 Ga (Zhang et al., 2015 and reference therein). U—Pb ages and Lu—Hf isotopic data for detrital zircons from the sedimentary cover sequences and the modern fluvial sand in the Ordos Block also support this opinion (Zhang et al., 2018). Nevertheless, limited drill holes are only distributed in the central and northeast Ordos Block (Zhang et al., 2015), and the heterogeneous of basement structures of Ordos Block were revealed by geophysical methods (Wang et al., 2015), both the composition and evolution history of the basement in the southwestern margin of the Ordos Block are still in the research gap stage.
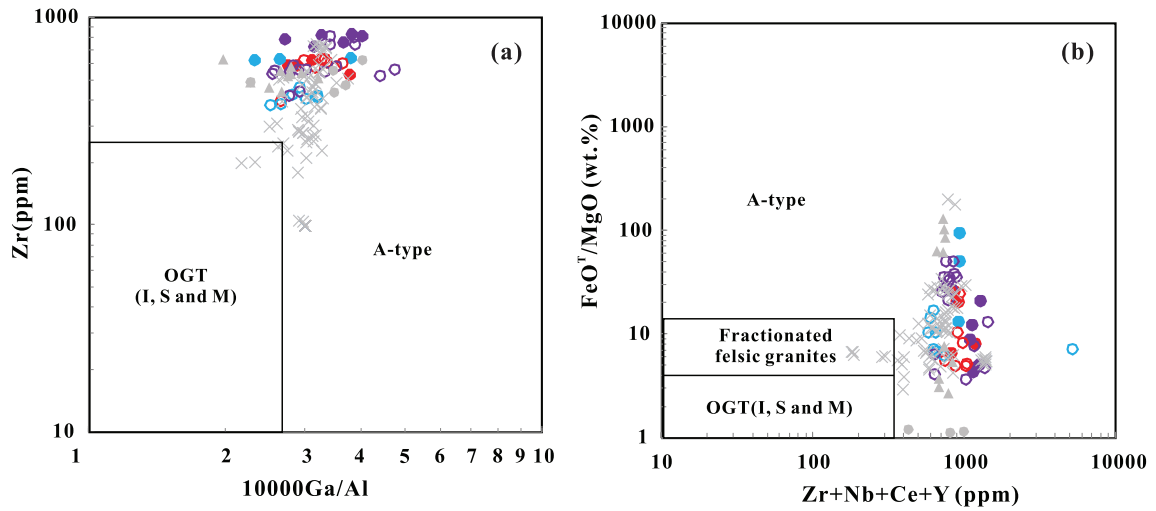
Fig. 13. (a) Zr (ppm) vs. 10,000 Ga/Al and (b) FeO^T/MgO vs. (Zr + Nb + Ce + Y) (ppm) diagrams of the Baijiagou, Shizuizi and Baojiashan rhyolites (after Whalen et al., 1987). Symbols as in Fig. 8.
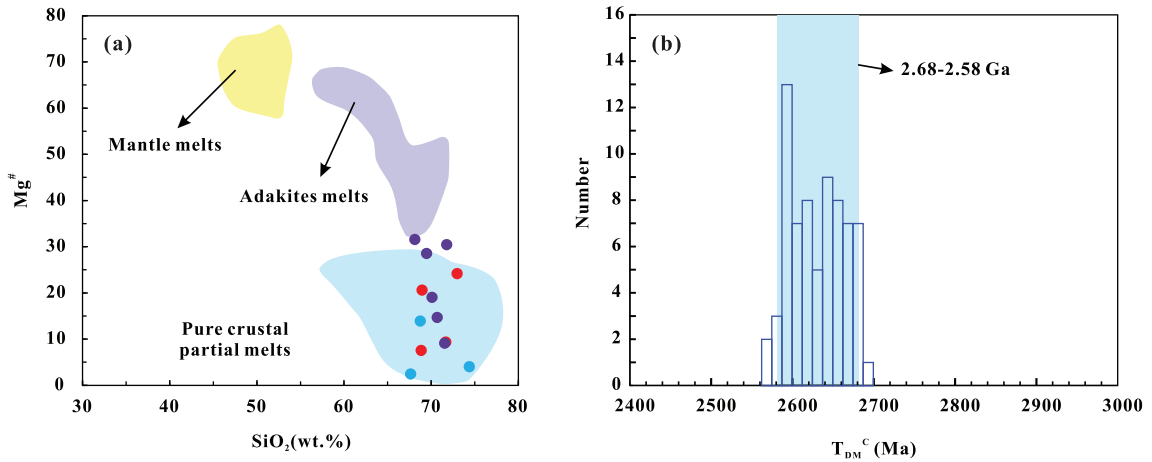

Fig. 14. (a) Diagram of Mg$^#$ vs. SiO$_2$ (wt%) for samples of the Baijiagou, Shizuizi, and Baojiashan rhyolites. Symbols as in Fig. 8. Melt compositions are from Rapp et al. (1999) and Smithies (2000). (b) Binned frequency histograms of T_{DM}^C.
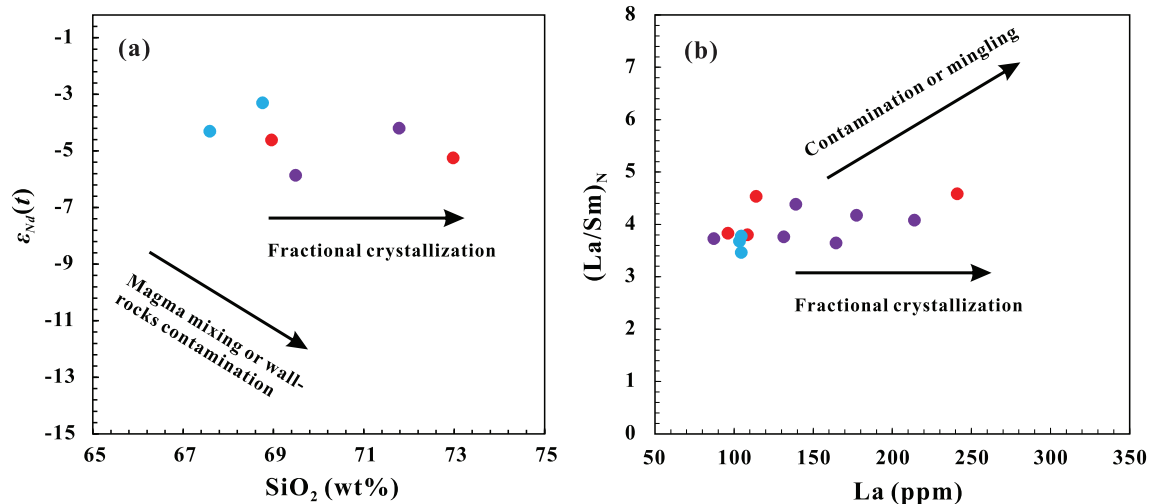

Fig. 15. $\varepsilon_{Nd}(t)$ vs. SiO$_2$ (wt%) (a) and (La/Sm)$_N$ vs. La (ppm) (b) for samples of the Baijiagou, Shizuizi, and Baojiashan rhyolites. Symbols as in Fig. 8.

Both the A-type rhyolites in this study and their contemporaneous A-type granites in the southern margin of the NCC were all derived from partial melting of felsic crustal materials (Cui et al., 2013; Deng et al., 2016; Shi et al., 2017; Zhao and Zhou, 2009). It should be noted that their whole-rock Sm—Nd and zircon Lu—Hf isotope are different between them, characterized by lower $\varepsilon_{Hf}(t)$ and $\varepsilon_{Nd}(t)$ values and older two-stage model ages of A-type granites in the southern margin of the NCC (Fig. 11), indicating different source nature. The two-stage Hf model ages of the A-type granites in the southern margin of the NCC are 3.2–2.7 Ga, mainly concentrated in 2.9–2.7 Ga, which is consistent with the main crustal growth stage in the southern NCC, while that of the rhyolites in this study are 2.70–2.57 Ga, most concentrated in 2.68–2.58 Ga (Fig. 14b), indicating a crustal growth or recycling of ancient continent crust at the middle Neoarchean time in the southwestern NCC.

6.3. Tectonic setting and implication

It is generally considered that A-type granites/rhyolites were formed in extensional settings, such as post-collisional/post-orogenic or anorogenic (e.g., rift, mantle plume) environments although their petrogenesis is still debated (e.g., King et al., 1997; Whalen et al., 1987). However, it is difficult to address the specific tectonic setting of A-type granites/rhyolites because of their similar lithology, mineralogy, and geochemistry (Sylvester, 1998).

Recently, Hu et al. (2016) propose that the south-western part of the NCC might develop a Guyuan Rift which is similar to Xiong'er Rift during the late Paleoproterozoic to Neoproterozoic according to the drill well data, seismic profiles, and sporadic outcrops, and considered that the south-western part of NCC share similar tectonic background with Xiong'er Rift. Felsic rocks derived from juvenile materials generally display positive $\varepsilon_{Hf}(t)$ and $\varepsilon_{Nd}(t)$ values and are genetically related to post-collisional/post-orogenic settings (Goodge and Vervoort, 2006). Nevertheless, the ~1.79 Ga A-type rhyolites in this study show negative $\varepsilon_{Hf}(t)$ and $\varepsilon_{Nd}(t)$ values and old two-stage model ages which are opposite to rocks from post-collisional/post-orogenic settings, suggesting they were probably formed in rift setting. Meanwhile, the late Paleoproterozoic rift-related diabase have been identified in the study area (Xu et al., 2019). The diabase and A-type rhyolites collectively represent a late Paleoproterozoic bimodal magmatic assemblage, indicate that the southwestern margin of the NCC was in a rift tectonic setting in the late Paleoproterozoic. There are also mafic dyke swarms with ages of ca. 1.78 Ga in the Xiong'er region and Lvliang-Taihang of the NCC (Peng et al., 2008), indicating widespread rift-related events occurred at this time. The southern margin of the NCC developed a large scale of late Paleoproterozoic volcano-sedimentary rocks and ca. 1.78–1.60 Ga anorogenic magmatism (e.g., Wang et al., 2010; Zhai et al., 2015), developing Xiong'er Rift along the southern margin of the NCC. In this regard, the rift-setting was widespread during the late Paleoproterozoic. Of the three series of A-type rhyolites, the earliest rift-related magmatism identified in the southwestern margin of NCC after the Paleoproterozoic consolidation of the crystalline basement, suggest that the intracontinental rift started as early as ca. 17.9 Ga.

The Xiong'er rift was caused by a mantle plume, which is characterized by the 1.78 Ga Large Igneous Province, including the Xiong'er volcanic rocks and the contemporaneous mafic dyke swarms (Peng et al., 2008). The late Paleoproterozoic magmatic events related to rifting developed in the southwestern margin of the NCC did not constitute a large igneous province. It is likely that they were influenced by the mantle plume in the south margin of the NCC, which caused the asthenosphere upwelling in the southwestern margin of the NCC and further led to the uplift, lithosphere thinning, and the development of a rift system.

The Paleoproterozoic is regarded as a critical period of assembly and breakup of the Columbia supercontinent (e.g., Ernst et al., 2008; Wu et al., 2018). The Columbia supercontinent assembly is recorded by the 2.0–1.8 Ga collisional orogenic belts, including the Trans-North

China Orogen and the Khondalite Belt in the NCC (Zhao et al., 2012). The late Paleoproterozoic orogenic events of the NCC are exemplified by the two-stage metamorphism of the greenschist-amphibolite facies during 1.91–1.85 Ga, and large-scale magmatism, such as 1.88–1.82 Ga mafic intrusive rocks, syenites and A-type granites in the Jiao-Liao-Ji Belt, 1.87–1.85 Ga charnockite in the southern NCC, as well as 1.85 Ga granodiorite granite, mafic dyke swarms and 1.88–1.85 Ga S-type granite in the Khondalite Belt (Yin et al., 2011; Zhao and Zhai, 2013).

Subsequently, large volumes of post-orogenic magmatic rocks were generated during ca.1.85–1.79 Ga, including the mafic dyke swarms, A-type granites, and minor S-type granites. The 1.85–1.79 Ga mafic dyke swarms include Mengyin diabasic dyke (1841 ± 17 Ma, Wang et al., 2007) and Taishan diabasic dyke (1837 ± 18 Ma, Hou et al., 2006). The contemporaneous post-orogenic A-type granites were widely distributed in the NCC, such as the Yunzhongshan and Luyashan plutons in the central NCC, the Yuantou, Motianzhai, Guijiayu, Shangdian and Dengfeng plutons in the southern part of the NCC (Deng et al., 2016; Geng et al., 2004; Shi et al., 2017; Zhao and Zhou, 2009). Also, a few S-type granites in post-orogenic setting developed in the khondalite belt (1840 ± 15 Ma and 1858 ± 23 Ma, Yin et al., 2011). Moreover, the latest retrograde metamorphism of the NCC occurred at 1.80–1.79 Ga, for example, the ages of amphibole, plagioclase, and biotite in the metamorphic rock series in the northern NCC are 1794 ± 17 Ma, 1798 ± 2 Ma, and 1782 ± 3 Ma, respectively (Wang et al., 1995); the metamorphic age of high-pressure granulite in Sanggan, the garnet mafic granulite in northern Hebei Province, and gneiss in Huai'an Terrane is 1792 ± 14 Ma (Zhang et al., 2006), 1793 ± 4 Ma (Liu et al., 2007), and 1786 ± 12 Ma (Liu et al., 2009b), respectively. The above data indicate that the overall tectonic setting of the NCC in ca.1.85–1.79 Ga was post-orogenic.

The NCC evolved into the intracontinental extension after ca. 1.79 Ga, as indicated by the rift-related magmatism and sedimentary sequences. The early magmatic activity is ca. 1.78 Ga magmatism, such as the Xiong'er volcanic rocks, Taihang-Lvliang mafic dyke swarms, Zhuyangcha hornblende quartz monzonites, and A-type rhyolites in this study (e.g., Peng et al., 2008). Most researchers proposed that the extensional continental rift environment resulted from the upwelling of a mantle plume (e.g., Peng et al., 2008; Zhai et al., 2015; Zhao et al., 2002). In combination with the regional geology and three localities of the rhyolites in this study, the NCC may have changed from post-orogenic stage to intracontinental rifting at ca. 1.79 Ga.

7. Conclusion

(1) The Baijiagou, Shizuizi, and Baojiashan rhyolites belonged to rhyolites of extrusive facies rather than granites of intrusive facies previously considered.

(2) The rhyolites from the southwestern margin of the NCC were formed at ca. 1795–1780 Ma. They were synchronous with the peak magmatism of the Xiong'er volcanic rocks.

(3) The rhyolites show geochemical compositions of A-type granite. They were produced by partial melting of the Neoarchean felsic basement rocks, which had experienced high-T hydrothermal alteration before melting.

(4) The rhyolites were formed in a rift environment, marking the initial rift in the southwestern margin of the NCC and transition from post-orogenic into intracontinental rift setting at ca. 1.79 Ga.

Declaration of Competing Interest

The authors declare that they have no known competing financial interests or personal relationships that could have appeared to influence the work reported in this paper.

Acknowledgments

References

Bindeman, I.N., Valley, J.W., 2002. Oxygen isotope study of the Long Valley magma system, California: isotope thermometry and convection in large silicic magma bodies. Contrib. Mineral. Petrol. 144, 185–205.

Cawood, P.A., Hawkesworth, C.J., 2014. Earth's middle age. Geology 42, 503–506.

Chappell, B.W., 1999. Aluminium saturation in I and S-type granites and the characterization of fractionated haplogranites. Lithos 46, 535–551.

Che, Z.C., Wang, R.S., 1985. An investigation on Cenozoic volcanism in Weihe Basin. J. Northwest Univ. 49, 82–88 (in Chinese with English abstract).

Creaser, R.A., Price, R.C., Wormald, R.J., 1991. A-type granites revisited: Assessment of a residual-source model. Geology 19, 163–166.

Cui, M.L., Zhang, L.C., Zhang, B.L., Zhu, M.T., 2013. Geochemistry of 1.78 Ga A-type granites along the southern margin of the North China Craton: implications for Xiong'er magmatism during the break-up of the supercontinent Columbia. Int. Geol. Rev. 55, 496–509.

Deng, X.Q., Peng, T.P., Zhao, T.P., 2016. Geochronology and geochemistry of the late Paleoproterozoic aluminous A-type granite in the Xiaoqinling area along the southern margin of the North China Craton: Petrogenesis and tectonic implications. Precambrian Res. 285, 127–146.

Drüppel, K., McCready, A.J., Stumpfl, E.F., 2009. High-K granites of the Rum Jungle complex, N-Australia: insights into the late Archean crustal evolution of the North Australian Craton. Lithos 111, 203–219.

Ernst, R.E., Wingate, M.T.D., Buchan, K.L., Li, Z.X., 2008. Global record of 1600–700Ma large Igneous Provinces (LIPs): implications for the reconstruction of the proposed Nuna (Columbia) and Rodinia supercontinents. Precambrian Res. 160, 159–178.

Frost, B.R., Barnes, C.G., Collins, W.J., Arculus, R.J., Ellis, D.J., Frost, C.D., 2001. A geochemical classification for granitic rocks. J. Petrol.J. Petrol. 42, 2033–2048.

Gao, S.L., Lin, J.Y., Lu, Y.J., 2013. Formation epoch and its geological implications of Paleoproterozoic A-type granite in Shizuizi of Jingyuan County, Ningxia Province. Acta Petrol. Sin. 29, 2676–2684 (in Chinese with English abstract).

Geng, Y.S., Yang, C.H., Song, B., Wan, Y.S., 2004. Post-orogenic granites with an age of 1800 Ma in Luliang area, North China Craton: constraints from isotopic geochronology and geochemistry. Geol. J. China Univ. 10, 477–487 (in Chinese with English abstract).

Goodge, J.W., Vervoort, J.D., 2006. Origin of Mesoproterozoic A-type granites in Laurentia: Hf isotope evidence. Earth Planet. Sci. Lett. 243, 711–731.

Griffin, W.L., Wang, X., Jackson, S.E., Pearson, N.J., O'Reilly, S.Y., Xu, X.S., Zhou, X.M., 2002. Zircon chemistry and magma mixing, SE China: in-situ analysis of Hf isotopes, Tonglu and Pingtan igneous complexes. Lithos 61, 237–269.

Han, S.X., Wu, C., Zhou, Z.G., Wang, G.S., 2020. Geology, geochemistry, and geochronology of the paleoproterozoic donggouzi mafic-ultramafic complex: implications for the evolution of the North China craton. Lithos 366-367, 105567.

Hildreth, W., Christiansen, R.L., O'Neil, J.R., 1984. Catastrophic isotopic modification of rhyolitic magma at times of caldera subsidence, Yellowstone Plateau volcanic field. J. Geophys. Res. 89, 8339–8369.

Hou, G.T., Wang, C.C., Li, J.H., Qian, X.L., 2006. Late Paleoproterozoic extension and a paleostress field reconstruction of the North China Craton. Tectonophysics 422, 89–98.

Hu, Z.C., Liu, Y.S., Gao, S., Liu, W., Yang, L., Zhang, W., Tong, X., Lin, L., Zong, K.Q., Li, M., Chen, H., Zhou, L., 2012. Improved in situ Hf isotope ratio analysis of zircon using newly designed X skimmer cone and Jet sample cone in combination with the addition of nitrogen by laser ablation multiple collector ICP-MS. J. Anal. At. Spectrom. 27, 1391–1399.

Hu, J.M., Gong, W.B., Wu, S.J., Liu, Y., Liu, S.C., 2014. LA-ICP-MS zircon U–Pb dating of the Langshan Group in the northeast margin of the Alxa block, with tectonic implications. Precambrian Res. 255, 756–770.

Hu, Z.C., Zhang, W., Liu, Y.S., Gao, S., Li, M., Zong, K.Q., Chen, H.H., Hu, S.H., 2015. "Wave" signal-smoothing and mercury-removing device for laser ablation quadrupole and multiple collector ICPMS analysis: application to lead isotope analysis. Anal. Chem. 87, 1152–1157.

Hu, J.M., Li, Z.H., Gong, W.B., Hu, G.H., Dong, X.P., 2016. Meso-neoproterozoic stratigraphic and tectonic framework of the North China Craton. In: Zhai, M.G., Zhao, Y., Zhao, T.P. (Eds.), Main Tectonic Events and Metallogeny of the North China Craton. Springer, Singapore, pp. 393–422.

Huang, H.Q., Li, X.H., Li, W.X., Li, Z.X., 2011. Formation of high δ18O fayalite-bearing A-type granite by high-temperature melting of granulitic metasedimentary rocks, southern China. Geology 39, 903–906.

Huang, D.L., Wang, X.L., Xia, X.P., Wan, Y.S., Zhang, F.F., Li, J.Y., Du, D.H., 2019. Neoproterozoic low-δ18O Zircons Revisited: Implications for Rodinia Configuration. Geophys. Res. Lett. 46, 678–688.

King, P.L., White, A.J.R., Chappell, B.W., Allen, C.M., 1997. Characterization and origin of aluminous A-type granites from the Lachlan Fold Belt, southeastern Australia. J. Petrol.J. Petrol. 38, 371–391.

King, P.L., Chappell, B.W., Allen, C.M., White, A.J.R., 2001. Are A-type granites the high-temperature felsic granites? Evidence from fractionated granites of the Wangrah Suite Australian. J. Earth Sci. 48, 501–514.

Kusky, T.M., Mooney, W.D., 2015. Is the Ordos basin floored by a trapped oceanic plateau? Earth Planet. Sci. Lett. 429, 197–204.

Larson, P.B., Geist, D.J., 1995. On the origin of low-18O magmas: evidence from the Casto pluton, Idaho. Geology 23, 909–912.

Li, X.H., Li, Z.X., Wingate, M.T.D., Chung, S.L., Liu, Y., Lin, G.C., Li, W.X., 2006. Geochemistry of the 755Ma Mundine well dyke swarm, northwestern Australia: part of a Neoproterozoic mantle superplume beneath Rodinia? Precambrian Res. 146, 1–15.

Li, X.H., Liu, Y., Li, Q.L., Guo, C.H., Chamberlain, K.R., 2009. Precise determination of Phanerozoic zircon Pb/Pb by multicollector SIMS without external standardization. Geochem. Geophys. Geosyst. 10.

Li, X.H., Long, W.G., Li, Q.L., Liu, Y., Zheng, Y.F., Yang, Y.H., Chamberlain, K.R., Wan, D.F., Guo, C.H., Wang, X.C., 2010. Penglai zircon megacrysts: a potential new working reference material for microbeam determination of Hf–O isotopes and U–Pb age. Geostand. Geoanal. Res. 34, 117–134.

Li, X.H., Tang, G.Q., Gong, B., Yang, Y.H., Hou, K.J., Hu, Z.C., Li, Q.L., Liu, Y., Li, W.X., 2013. Qinghu zircon: a working reference for microbeam analysis of U-Pb age and Hf and O isotopes. Chin. Sci. Bull. 58, 4647–4654.

Liu, S.W., Lv, Y.J., Feng, Y.G., Zhang, C., Tian, W., Yan, Q.R., Liu, X.M., 2007. Geology and Zircon U-Pb Isotopic chronology of Dantazi complex, Northern Hebei Province. Geol. J. China Univ. 13, 484–497 (in Chinese with English abstract).

Liu, D.Y., Wilde, S.A., Wan, Y.S., Wang, S.Y., Valley, J.W., Kita, N., Dong, C.Y., Xie, H.Q., Yang, C.X., Zhang, Y.X., Gao, L.Z., 2009a. Combined U–Pb, hafnium and oxygen isotope analysis of zircons from meta-igneous rocks in the southern North China Craton reveal multiple events in the late Mesoarchean–early Neoarchean. Chem. Geol. 261, 140–154.

Liu, F., Guo, J.H., Lu, X.P., Diwu, C.R., 2009b. Crustal growth at ~2.5 Ga in the North China Craton: evidence from whole-rock Nd and zircon Hf isotopes in the Huai'an gneiss terrane. Sci. Bull. 54, 4704–4713.

Liu, Y.S., Gao, S., Hu, Z.C., Gao, C.G., Zong, K.Q., Wang, D.B., 2010. Continental and Oceanic Crust Recycling-induced Melt-Peridotite Interactions in the Trans-North China Orogen: U-Pb Dating, Hf Isotopes and Trace elements in Zircons from Mantle Xenoliths. J. Petrol.J. Petrol. 51, 537–571.

Loiselle, M.C., Wones, D.R., 1979. Characteristics and origin of anorogenic granites. Geol. Soc. Am. Abstr. Programs 11, 468.

Ludwig, K.R., 2003. User's Manual for ISOPLOT 3.00: A Geochronological Toolkit for Microsoft Excel, Special Publication No. 4. Berkeley Geochronology Center, p. 71.

Maniar, P.D., Piccoli, P.M., 1989. Tectonic discrimination of granitoids. Geol. Soc. Am. Bull. 101, 635–643.

Patiño Douce, A.E., 1997. Generation of metaluminous A-type granites by low-pressure melting of calc-alkaline granitoids. Geology 25, 743–746.

Peng, P., Zhai, M.G., Ernst, R.E., Guo, J.H., Liu, F., Hu, B., 2008. A 1.78 Ga large igneous province in the North China craton: the Xiong'er Volcanic Province and the North China dyke swarm. Lithos 101, 260–280.

Rapp, R.P., Shimizu, N., Norman, M.D., Applegate, G.S., 1999. Reaction between slab-derived melts and peridotite in the mantle wedge: experimental constraints at 3.8 GPa. Chem. Geol. 160, 335–356.

Rudnick, R., Gao, S., 2003. The role of lower crustal recycling in continent formation. Geochimica et Cosmochimica Acta Suppl. 67, 403.

Shellnutt, J.G., Zhou, M.F., 2007. Permian peralkaline, peraluminous and metaluminous A-type granites in the Panxi district, SW China: their relationship to the Emeishan mantle plume. Chem. Geol. 243, 286–316.

Shi, J.P., Yang, D.B., Huo, P.F., Yang, H.T., Xu, W.L., Wang, F., 2017. The geochronology and Nd-Hf isotope composition of A-type granites on the sourthern margin of North China Croton: Constrains on the late Paleoproterozoic extensional events. Acta Petrol. Sin. 33 3402–3056 (in Chinese with English abstract).

Smithies, R.H., 2000. The Archaean tonalite-trondhjemite-granodiorite (TTG) series is not an analogue of Cenozoic adakite. Earth Planet. Sci. Lett. 182, 115–125.

Sun, S.S., McDonough, W.F., 1989. Chemical and isotopic systematics of oceanic basalts: Implication for mantle composition and processes. In: Sauders, A.D., Norry, M.J. (Eds.), Magmatism in the Ocean Basins. vol. 42. Geological Society Special Publication, UK, pp. 313–345.

Sylvester, P.J., 1998. Post-collisional strongly peraluminous granites. Lithos 45, 29–44.

Taylor, H.P., Sheppard, S.M.F., 1986. Igneous rocks; I, Processes of isotopic fractionation and isotope systematics. Rev. Mineral. Geochem. 16, 227–271.

Valley, W., 2003. Oxygen Isotopes in Zircon Reviews in Mineralogy and Geochemistry. 53 pp. 347–385.

Valley, J.W., Lackey, J.S., Cavosie, A.J., Clechenko, C.C., Spicuzza, M.J., Basei, M.A.S., Bindeman, I.N., Ferreira, V.P., Sial, A.N., King, E.M., Peck, W.H., Sinha, A.K., Wei, C.S., 2005. 4.4 billion years of crustal maturation: oxygen isotope ratios of magmatic zircon. Contrib. Mineral. Petrol. 150, 561–580.

Wang, J., Li, S.Q., Wang, B.L., Li, J.J., 1992. The Langshan-Bayan Obo Rift System. Press of Peking University, Beijing, pp. 1–132 (in Chinese).

Wang, S.S., Sang, H.Q., Qiu, J., Chen, M.G., Li, M.R., 1995. The metamorphic age of pre-Chancheng System in Beijing-Tianjin area and a discussion about the lower limit age of Changcheng System. Sci. Geol. Sin. 30, 348–354 (in Chinese with English abstract).

Wang, Y.J., Zhao, G.C., Fan, W.M., Peng, T.P., Sun, L.H., Xia, X.P., 2007. LA-ICP-MS U–Pb zircon geochronology and geochemistry of Paleoproterozoic mafic dykes from western Shandong Province: implications for back-arc basin magmatism in the Eastern Block, North China Craton. Precambrian Res. 154, 107–124.

Wang, X.L., Jiang, S.Y., Dai, B.Z., 2010. Melting of enriched Archean subcontinental lithospheric mantle: evidence from the ca. 1760Ma volcanic rocks of the Xiong'er Group, southern margin of the North China Craton. Precambrian Res. 182, 204–216.

Wang, X.C., Li, Z.X., Li, X.H., Li, Q.L., Tang, G.Q., Zhang, Q.R., Liu, Y., 2011. Nonglacial origin for low- [18]O Neoproterozoic magmas in the South China Block: evidence from new in-situ oxygen isotope analyses using SIMS. Geology 39, 735–738.

Wang, Z.T., Zhou, H.R., Wang, X.L., Jing, X.C., 2015. Characteristics of the crystalline basement beneath the Ordos Basin: Constraint from aeromagnetic data. Geosci. Front. 6, 465–475.

Wang, X.Y., Qin, J.F., Lai, S.C., Long, X.P., Ju, Y.J., Zhang, Z.Z., Zhu, R.Z., 2019. Paleoproterozoic a type granite from the southwestern margin of the North China block high temperature melting of tonalitic crust in extensional. Int. Geol. Rev.Int. Geol. Rev. 62, 614–629.

Watson, E.B., Harrison, T.M., 1983. Zircon saturation revisited: temperature and composition effects in a variety of crustal magma types. Earth Planet. Sci. Lett. 64, 295–304.

Whalen, J.B., Currie, K.L., Chappell, B.W., 1987. A-type granites: geochemical characteristics, discrimination and petrogenesis. Contrib. Mineral. Petrol. 95, 407–419.

Wilson, M., 1989. Igneous Petrogenesis: A Global Tectonic Approach. Chapman and Hall, London, pp. 13–34.

Wu, C., Zhou, Z.G., Zuza, A.V., Wang, G.S., Liu, C.F., Jiang, T., 2018. A 1.9-Ga Mélange along the northern margin of the North China Craton: implications for the assembly of Columbia Supercontinent. Tectonics 37, 3610–3646.

Xu, H., Zhao, H., Luo, J.H., Cheng, J.X., You, J., Wang, S.D., 2014. Paleoproterozoic granite and its tectonic significances in Southwestern margin of North China Plate, Baojiashan Section in Longxian County. Geol. Rev. 60, 1284–1296 (in Chinese with English abstract).

Xu, H., Luo, J.H., Chen, G.X., You, J., Li, Y.F., 2019. Geochronology, geochemistry and tectonic significance of a Paleoproterozoic diabase at southwestern margin of the NCC. Terr. Atmos. Ocean. Sci. 30, 771–791.

Xue, S., Xu, Y., Ling, M.X., Kang, Q.Q., Jiang, X.Y., Sun, S.J., Wu, K., Zhang, Z.K., Luo, Z.B., Liu, Y.L., Sun, W.D., 2018. Geochemical constraints on genesis of Paleoproterozoic A-type granite in the south margin of North China Craton. Lithos 304-307, 489–500.

Yang, J.H., Wu, F.Y., Chung, S.L., Wilde, S.A., Chu, M.F., 2006. A hybrid origin for the Qianshan A-type granite, Northeast China: geochemical and Sr–Nd–Hf isotopic evidence. Lithos 89, 89–106.

Yin, C.Q., Zhao, G.C., Guo, J.H., Sun, M., Xia, X.P., Zhou, X.W., Liu, C.H., 2011. U–Pb and Hf isotopic study of zircons of the Helanshan complex: constrains on the evolution of the Khondalite Belt in the Western Block of the North China Craton. Lithos 122, 25–38.

You, J., Luo, J.H., Cheng, J.X., Wang, S.D., Xu, H., Zhao, H., 2014. Paleoproterozoic Granite Porphyry in Southwestern margin of North China Craton and its Geological significance. Geol. J. China Univ. 20, 368–377 (in Chinese with English abstract).

Zhai, M.G., Santosh, M., 2011. The early Precambrian odyssey of the North China Craton: a synoptic overview. Gondwana Res. 20, 6–25.

Zhai, M.G., Hu, B., Zhao, T.P., Peng, P., Meng, Q.R., 2015. Late Paleoproterozoic–Neoproterozoic multi-rifting events in the North China Craton and their geological significance: a study advance and review. Tectonophysics 662, 153–166.

Zhang, S.B., Zheng, Y.F., 2011. On the orign of low δ^{18}O magmatic rocks. Acta Petrol. Sin. 27, 520–530 (in Chinese with English abstract).

Zhang, H.F., Zhai, M.G., Peng, P., 2006. Zircon SHRIMP U-Pb age of the Paleoproterozoic high-pressure granulites from the Sanggan area, the North China Craton and its geologic implications. Earth Sci. Front. 13, 190–199 (in Chinese with English abstract).

Zhang, S.H., Liu, S.W., Zhao, Y., Yang, J.H., Song, B., Liu, X.M., 2007. The 1.75–1.68Ga anorthosite-mangerite-alkali granitoid-rapakivi granite suite from the northern North China Craton: Magmatism related to a Paleoproterozoic orogen. Precambrian Res. 155, 287–312.

Zhang, C.L., Diwu, C.R., Kröner, A., Sun, Y., Luo, J.L., Li, Q.L., Gou, L.L., Lin, H.B., Wei, X.S., Zhao, J., 2015. Archean-Paleoproterozoic crustal evolution of the Ordos Block in the North China Craton: Constraints from zircon U–Pb geochronology and Hf isotopes for gneissic granitoids of the basement. Precambrian Res. 267, 121–136.

Zhang, C.L., Gou, L.L., Diwu, C.R., Liu, X.Y., Zhao, J., Hu, Y.H., 2018. Early Precambrian geological events of the basement in Western Block of North China Craton and their properties and geological significance. Acta Petrol. Sin. 34, 981–998 (in Chinese with English abstract).

Zhao, G.C., Zhai, M.G., 2013. Lithotectonic elements of Precambrian basement in the North China Craton: review and tectonic implications. Gondwana Res. 23, 1207–1240.

Zhao, T.P., Zhou, M.F., 2009. Geochemical constraints on the tectonic setting of Paleoproterozoic A-type granites in the southern margin of the North China Craton. J. Asian Earth Sci. 36, 183–195.

Zhao, G.C., Wilde, S.A., Cawood, P.A., Sun, M., 2001. Archean blocks and their boundaries in the North China Craton: lithological, geochemical, structural and P-T path constraints and tectonic evolution. Precambrian Res. 107, 45–73.

Zhao, T.P., Zhou, M.F., Zhai, M.G., Xia, B., 2002. Paleoproterozoic Rift-Related Volcanism of the Xiong'er Group, North China Craton: Implications for the Breakup of Columbia. Int. Geol. Rev.Int. Geol. Rev. 44, 336–351.

Zhao, G.C., Cawood, P.A., Li, S.Z., Wilde, S.A., Sun, M., Zhang, J., He, Y.H., Yin, C.Q., 2012. Amalgamation of the North China Craton: Key issues and discussion. Precambrian Res. 222-223, 55–76.

Zheng, Y.F., Wu, Y.B., Chen, F.K., Gong, B., Li, L., Zhao, Z.F., 2004. Zircon U-Pb and oxygen isotope evidence for a large-scale [18]O depletion event in igneous rocks during the Neoproterozoic. Geochim. Cosmochim. Acta. 68, 4145–4165.